Cell Reports

Resource

ULK1 phosphorylation of striatin activates protein phosphatase 2A and autophagy

Graphical abstract

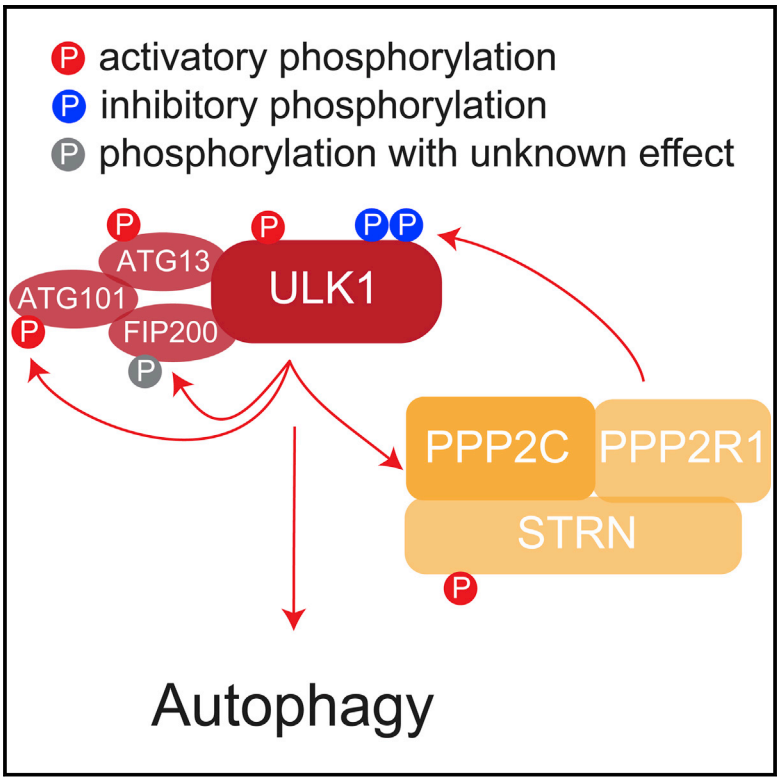

Highlights

- ULK1 regulates autophagosome expansion, maturation, and lysosomal fusion
- ULK1 regulates an elaborate protein phosphatase network
- ULK1 and striatin are linked by a regulatory feedback mechanism
- Phosphorylation of striatin by ULK1 promotes functional autophagy

Authors

Zehan Hu, Devanarayanan Siva Sankar, Bich Vu, ..., Esther Martínez-Martínez, Björn Stork, Jörn Dengjel

Correspondence

joern.dengjel@unifr.ch

In brief

By combining *in vivo* phosphoproteomics with whole-proteome, on-bead *in vitro* kinase assays, Hu et al. highlight a network of protein phosphatases, including members of the STRIPAK complex, which are regulated by ULK1 and critical for functional autophagy.

Hu et al., 2021, Cell Reports *36*, 109762
September 28, 2021 © 2021 The Author(s).
https://doi.org/10.1016/j.celrep.2021.109762

CellPress

Cell Reports

CellPress
OPEN ACCESS

Resource

ULK1 phosphorylation of striatin activates protein phosphatase 2A and autophagy

Zehan Hu,[1] Devanarayanan Siva Sankar,[1] Bich Vu,[1] Alexandre Leytens,[1] Christine Vionnet,[1] Wenxian Wu,[2] Michael Stumpe,[1] Esther Martínez-Martínez,[1] Björn Stork,[2] and Jörn Dengjel[1,3,*]

[1]Department of Biology, University of Fribourg, 1700 Fribourg, Switzerland

[2]Institute of Molecular Medicine I, Medical Faculty, Heinrich Heine University, 40225 Düsseldorf, Germany

[3]Lead contact

*Correspondence: joern.dengjel@unifr.ch

https://doi.org/10.1016/j.celrep.2021.109762

SUMMARY

The evolutionarily conserved ULK1 kinase complex acts as gatekeeper of canonical autophagy and regulates induction of autophagosome biogenesis. To better understand control of ULK1 and analyze whether ULK1 has broader functions that are also linked to the later steps of autophagy, we perform comprehensive phosphoproteomic analyses. Combining *in vivo* with *in vitro* data, we identify numerous direct ULK1 target sites within autophagy-relevant proteins that are critical for autophagosome maturation and turnover. In addition, we highlight an intimate crosstalk between ULK1 and several phosphatase complexes. ULK1 is not only a PP2A target but also directly phosphorylates the regulatory PP2A subunit striatin, activating PP2A and serving as positive feedback to promote autophagy-dependent protein turnover. Thus, ULK1 and phosphatase activities are tightly coordinated to robustly regulate protein degradation by autophagy.

INTRODUCTION

Macroautophagy, hereafter referred to as autophagy, summarizes constitutive and stimulus-dependent lysosomal degradation pathways that are critical for cell homeostasis (Dikic and Elazar, 2018; Mizushima and Levine, 2020). In general, autophagy acts cytoprotective and is often found dysregulated in human diseases, including metabolic diseases like cancer and metabolic syndrome (Mizushima and Levine, 2020). The hallmark of autophagy is the formation of a double membrane vesicle, the autophagosome. Autophagosome turnover is a hierarchical process and can be classified into five distinct steps: initiation by formation of a cup-shaped membrane, called phagophore, followed by elongation, maturation, closure, and finally fusion with endosomes and lysosomes leading to the formation of autolysosomes (Mintern and Villadangos, 2012; Nakatogawa, 2020).

Autophagosome initiation is regulated by two evolutionary conserved kinase complexes: (1) the protein kinase ULK1/2 complex (Chan et al., 2007), which activates, among others, (2) the VPS34 lipid kinase complex, a class III phosphatidylinositol 3-kinase complex (PtdIns3K), which generates phosphatidylinositol-3-phosphate that serves as docking site for further protein recruitment (Nakatogawa, 2020; Siva Sankar and Dengjel, 2020). ULK1 (or its homolog ULK2) is a Ser/Thr kinase forming a tetrameric complex with ATG13, ATG101, and RB1CC1/FIP200 (McAlpine et al., 2013; Zachari and Ganley, 2017). Upon cell stress, ULK1 is activated, phosphorylating itself and its complex members. This leads to endoplasmic reticulum (ER) recruitment of the complex and the formation of active phagophore initiation sites through direct interactions with ER membrane proteins VAPA/VAPB (vesicle-associated proteins A/B) (Zhao et al., 2018). VAPs interact with WD repeat-containing protein WIPI2, which in turn forms a tethering complex strengthening ER-phagophore contact sites, making ER essential for autophagosome biogenesis. WIPI proteins are, among others, important for the recruitment of the lipid transferase ATG2, and they control the size of autophagosomes (Bakula et al., 2017; Valverde et al., 2019). ULK1-dependent activation of the VPS34 complex happens via phosphorylation of complex members AMBRA1 (Di Bartolomeo et al., 2010), PIK3C3/VPS34 (Di Bartolomeo et al., 2010; Egan et al., 2015), PIK3R4/VPS15 (Gwinn et al., 2008; Mercer et al., 2021), BECN1 (Russell et al., 2013), and ATG14 (Wold et al., 2016). In contrast to the well-understood function of ULK1 in autophagy initiation, its role in later stages of the process is less clear. Interestingly, its yeast homolog Atg1 has also recently been shown to phosphorylate proteins that are important in autophagosome maturation and autophagosome-lysosome fusion, indicating that the function of ULK1 in autophagy regulation might be more complex than anticipated (Barz et al., 2020; Gao et al., 2020; Hu et al., 2019).

The major inhibitory kinase complex of autophagy functioning upstream of ULK1 is the mechanistic target of rapamycin complex 1 (mTORC1), which phosphorylates and inhibits ULK1 and ATG13 under nutrient-rich conditions (Ganley et al., 2009; Hosokawa et al., 2009; Jung et al., 2009). To activate ULK1, inhibitory mTORC1 phosphorylation sites, among others, on Ser637 and Ser757 on murine ULK1 must be removed (Kim et al., 2011; Shang et al., 2011). Amino acid starvation leads to protein phosphatase 2A (PP2A)-dependent dephosphorylation of Ser637 of ULK1 (Wong et al., 2015), whereas genotoxic stress leads to protein phosphatase 1D (PPM1D)-dependent dephosphorylation of the

This is an open access article under the CC BY license (http://creativecommons.org/licenses/by/4.0/).

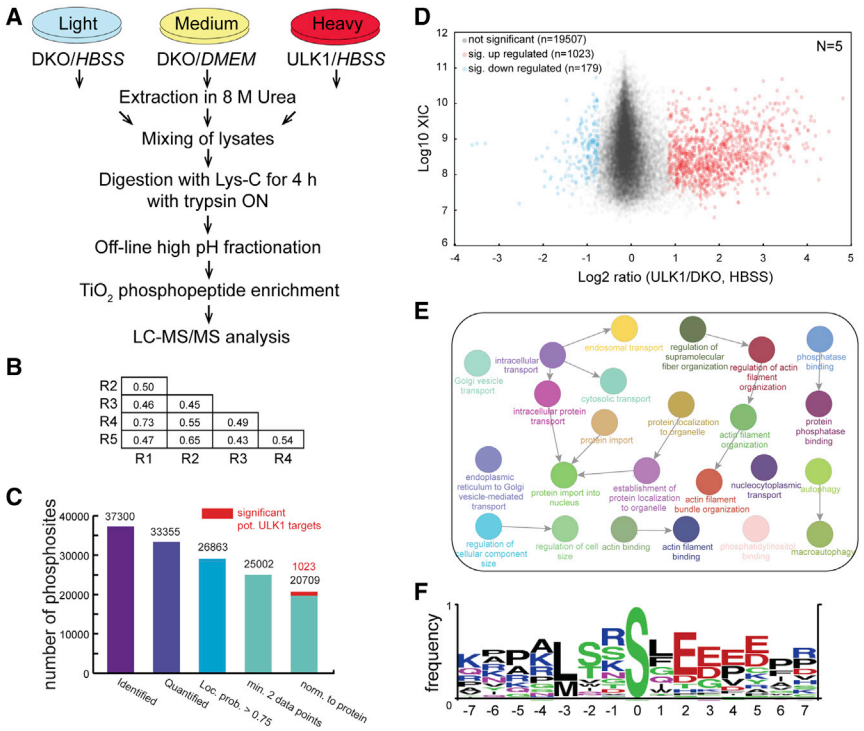

Figure 1. Global phosphoproteomic approach to identify ULK1-regulted phosphosites

(A) SILAC-based quantitative MS workflow. *Ulk1/ulk2* double knockout mouse embryonic fibroblasts (DKO MEFs) and *ulk1/ulk2* DKO MEFs expressing FLAG-tagged human ULK1 (ULK1 MEFs) were used to identify phosphosites potentially being regulated by ULK1. Cells kept in fed conditions (DMEM) were compared to starved cells kept for 1 h in Hank's balanced salt solution (HBSS).

(B) Correlation of biological replicates. Phosphorylation events in ULK1 MEFs were compared to events in DKO MEFs, both starved in HBSS for 1 h. Five biological replicates were performed. Shown are Person correlation coefficients r.

(C) Data analysis pipeline. Number of identified and quantified phosphosites fulfilling the indicated criteria comparing ULK1 MEFs to DKO MEFs.

(D) Regulation of potential ULK1 target sites. Average intensities based on the summed extracted ion currents (XICs) of peptides carrying respective phosphosites in relation to the fold change of regulation (log2 SILAC ratio) are used to highlight significantly regulated sites (n = 5; $p < 0.05$; BH-corrected). Sites highlighted in red represent potential ULK1 target sites.

(E) Biological processes potentially regulated by ULK1. GO network of proteins carrying significantly positively regulated sites highlighted in (D).

(F) Motif analysis of significantly upregulated sites. Significantly upregulated phosphosites were used to generate a kinase motif, which nicely corresponds to the published ULK1 motif.

same site promoting ULK1 and with this autophagy activity (Torii et al., 2016). Glucose starvation was shown to induce ULK1 activity by protein phosphatase 1 (PPP1CA)-dependent dephosphorylation of Ser757 (Pyo et al., 2018). Thus, ULK1 has been shown to be a target of several phosphatase complexes; however, whether ULK1 also regulates phosphatase activity is largely unknown.

In the current study, we aimed to identify direct, bona fide ULK1 targets by performing sets of *in vivo* and *in vitro* phosphoproteomic experiments, in order to better understand ULK1 function in autophagy regulation. *In vitro* reactions were performed by a newly developed, highly multiplexed kinase assay using entire proteome as input. We identified numerous direct ULK1 target sites on proteins being important in later stages of autophagy, i.e., in autophagosome maturation and autophagosome-lysosome fusion. In addition, we characterized a network of phosphatases being regulated by ULK1 and highlight the function of one member of the network, striatin/STRN a regulatory PP2A subunit and member of evolutionary conserved striatin-interacting phosphatase and kinase (STRIPAK) complexes (Kück et al., 2019). ULK1 and PP2A-STRN are linked via a positive feedback loop critical for robust activation of autophagy.

RESULTS

In vivo phosphoproteomics identifies potential ULK1 target sites

To generate a comprehensive dataset of potential ULK1-dependent phosphorylation events *in vivo*, we employed mouse embryonic fibroblasts (MEFs) isolated from *ulk1/ulk2* double knockout (DKO) mice that were re-transfected with either an expression plasmid encoding FLAG-tagged human ULK1 or the respective empty plasmid as control (Wu et al., 2020). Briefly, MEFs were differentially labeled by stable isotope labeling by amino acids in cell culture (SILAC) and kept in full or starvation medium for 1 h (Figure 1A). Phosphopeptides were processed as outlined and analyzed by liquid chromatography-tandem mass spectrometry (LC-MS/MS) (Figure 1A; see STAR Methods for details). We performed five biological replicates with a decent correlation, considering the noise of phosphoproteomic experiments (Figure 1B), and identified a total of 37,300 phosphosites on 6,278 proteins (Figure 1C). Of these, 20,709 were used for further analyses, as they could be localized to specific amino acid residues, were quantified in minimally two biological replicates, and were normalized to respective protein abundances (Table S1).

To identify sites that exhibited a significant fold change in phosphorylation in starvation conditions due to the presence of ULK1, we utilized a random effect model, considering the variability among replicates, sites, and the number of replicates for each site ($p < 0.05$; Table S1) (Hu et al., 2019). In addition, we calculated an outlier significance score on the merged log2-transformed phosphosite ratio data according to Cox and Mann (2008) (significance A; $p < 0.05$; BH-corrected). Only sites fulfilling the significance criteria in both tests were further considered. This led to the identification of 1,023 significantly upregulated, potential ULK1 target sites: less than 5% of the entire

dataset (Figures 1C and 1D). Gene Ontology (GO) enrichment analyses of proteins carrying regulated phosphosites highlighted that proteins were involved in intracellular and vesicular transport and autophagy, indicating that our experimental strategy was successful (Figure 1E). In addition, neighboring residues of regulated sites matched well with the previously proposed ULK1 motif (Figure 1F), indicating that our data are of high quality and largely confirm current knowledge (Egan et al., 2015).

ULK1 regulates autophagosome turnover

To screen data for sites that are likely important for cellular phenotypes, we performed additional sets of SILAC-based quantitative phosphoproteomic experiments in MEFs and A549 human alveolar adenocarcinomic cells (Figure S1; biological replicates $n \geq 5$ for each set; Table S1). Cells were treated with rapamycin or starved for amino acids, with both treatments leading to an inhibition of mTORC1 and consequently activation of ULK1 and autophagy, and compared to cells grown in full medium, i.e., active mTORC1, as negative control. These experiments should highlight (1) evolutionary conserved regulated sites, which should more likely be phenotypically relevant and (2) sites that are responding to different autophagy-inducing stimuli, which are more likely of central importance for autophagy regulation. Compared to data of the genetic model shown in Figure 1, phosphorylation differences due to culture conditions led to overall smaller fold changes (Figure S1). Also, the overlap between datasets was small (Figure S1), and kinase motifs were more different from the published ULK1 motif (Figure S2) (Nettling et al., 2015), indicating that changes in culture conditions induce a broader, less specific cellular response involving additional kinases, and that autophagy regulation by ULK1 only plays a minor role in overall phosphorylation-based signaling under stress.

ULK1 was described to be important for autophagy initiation (Chan and Tooze, 2009), and in agreement, we identified numerous potential ULK1 target sites on proteins contributing to autophagosome biogenesis, such as integral ER proteins VAPA and VAPB, which contribute to ER-phagophore contact site formation and selective removal of ER by autophagy, and PIK3R4/VPS15, a regulatory subunit of the VPS34 complex (Figure 2) (Nthiga et al., 2020; Thoresen et al., 2010; Zhao et al., 2018). In addition, ULK1 appears to be involved in several feedback loops affecting mTORC1 and AMPK regulators, such as LAMTOR/Ragulator and metadherin/MTDH (Bar-Peled et al., 2012; Bhutia et al., 2010). However, we also identified potential ULK1 target sites on numerous proteins that are critical for autophagosome expansion, maturation, and autophagosome-lysosome fusion, including ESCRT and SNARE protein members (Figure 2). Of the 53 proteins carrying significantly dysregulated phosphosites and being involved in autophagy and/or vesicle trafficking, eight were already known to be ULK1 target proteins, and of the listed sites, five were already reported as ULK1 target sites (Figure 2) (Mercer et al., 2018, 2021). Thus, we conclude that we have significantly expanded the list of potential ULK1 targets and that, as similarly recently described for the yeast homolog Atg1 (Hu et al., 2019), the effects of ULK1 on autophagy regulation also appear to be more complex than anticipated, affecting not just its initiation but all steps of the process.

Whole-proteome, on-bead *in vitro* kinase assay identifies direct ULK1 targets

To be able to discriminate direct from indirect ULK1 effects, we developed a highly multiplexed on-bead *in vitro* kinase assay (OBIKA) using immobilized cell proteome under native conditions as the input for *in vitro* kinase reactions (Figure 3A). By immobilizing cell lysate on N-Hydroxysuccinimid (NHS)-activated Sepharose under native conditions, repeated buffer exchanges were possible to support respective *in vitro* reactions (Figure S3). Bound proteins were dephosphorylated by λ-phosphatase to reduce the abundance of endogenous phosphosites (Figure 3B). As native conditions were used, immobilized kinases were still active, as shown by the detection of increased phosphorylation events after the addition of ATP (Figure 3B). To discriminate phosphorylation events of the kinase-of-interest added exogenously from reactions catalyzed by endogenous kinases immobilized on beads, (quasi)covalent kinase inhibitors were used to permanently block endogenous kinase activities (Figures 3A and 3B; see STAR Methods for details).

We tested our setup by monitoring known phosphosites using site-specific antibodies coupled to western blot. The ULK1 target site Ser29 on ATG14 was only phosphorylated in the presence of exogenous, active wild-type ULK1 ($ULK1^{WT}$) (Park et al., 2016). The kinase dead variant of the enzyme ($ULK1^{KD}$) and heat-inactivated $ULK1^{WT}$ did not have this effect. In contrast, the MEK sites Thr202 and Tyr204 on ERK1 were phosphorylated by endogenous MEK immobilized on beads in the presence of ATP. The addition of kinase inhibitors blocked this phosphorylation event, and exogenous $ULK1^{WT}$ or $ULK1^{KD}$ did not significantly interfere with the phosphorylation of these sites (Figure 3C).

Next, we coupled this assay to label-free quantitative MS and compared assays in the presence of $ULK1^{WT}$ to (1) assays performed in the presence of $ULK1^{KD}$ and (B) assays performed without any exogenous kinase, both serving as negative controls. This led to the identification of 4,255 significantly regulated ULK1 target phosphosites on 2,458 proteins (Figure 3D; $p < 0.05$; BH-corrected; $n = 3$; Table S2). Analyzing phosphosites surrounding amino acids, the ULK1 motif was confirmed, supporting that the shortlisted sites were indeed direct ULK1 target sites (Figure 3E; Figure S2) (Egan et al., 2015). To identify ULK1 target sites of physiological relevance within the list of *in vitro* sites, we compared *in vitro* with *in vivo* data. We quantified 10,687 common sites by both approaches, of which a total of 1,924 sites were significantly regulated (Figure 3F). Of these, 187 sites on 157 proteins were significantly, positively regulated in both approaches, characterizing them as bona fide ULK1 target sites (Figure 3G; Table S3), among them several proteins already known to be important in autophagy but not having been characterized as ULK1 targets, such as VAPA, VAPB, and the E3 ligase HUWE1, which is important for the removal of mitochondria by autophagy (Figure 3F) (Di Rita et al., 2018; Nthiga et al., 2020; Zhao et al., 2018). Protein interaction analysis using STRING-DB generated a network of 118 out of the 157 shortlisted proteins, which carry GO terms associated to vesicle and ER-Golgi transport, indicating a potentially broader role of ULK1 (Figure S4) (Szklarczyk et al., 2019).

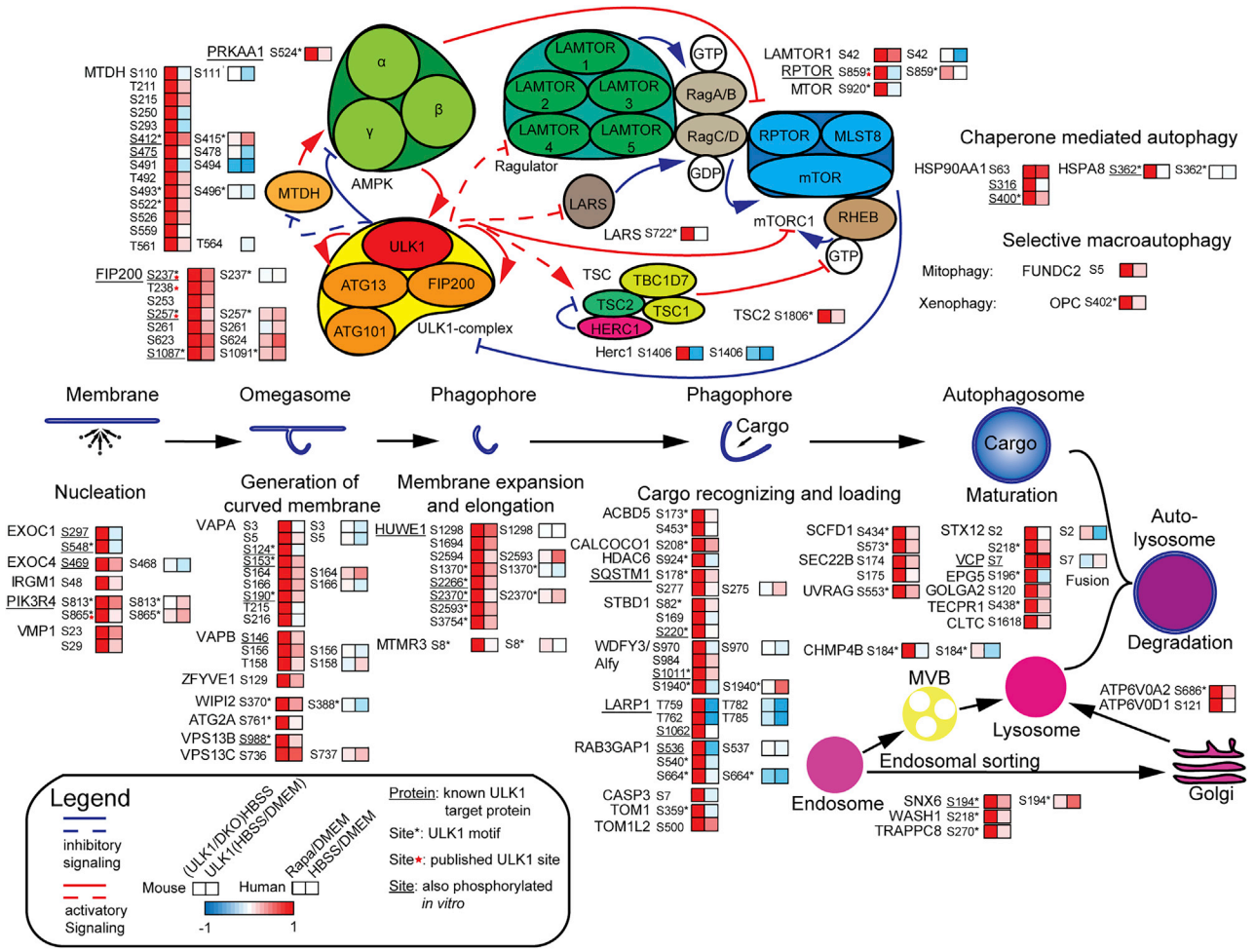

Figure 2. ULK1 regulates autophagosome turnover

Shown are proteins that have been linked to autophagy and were identified as carrying significantly upregulated, potential ULK1 phosphosites in (1) ULK1 compared to DKO MEFs (both for 1 h in HBSS; Figure 1). To identify potential *in vivo* relevant sites, three additional SILAC-based comparisons were performed comparing (2) ULK1 MEFs in HBSS to ULK1 MEFs in DMEM (n = 5), (3) A549 cells treated with rapamycin (Rapa) to untreated A549 cells in DMEM (n = 8), and (4) A549 cells in HBSS to A549 cells in DMEM (n = 8). Solid lines indicate known interactions/signaling events. Dashed lines indicate predicted interactions/signaling events by the current data.

ULK1 regulates phosphatase activity

Comparing regulated phosphosites due to changes in cell culture conditions, i.e., starved/rapamycin-treated versus non-starved/non-treated conditions, we noticed that similar numbers of sites were significantly down- and upregulated (Figure S1). In our setting, downregulation of sites may reflect the inhibition of the master regulator of cell growth mTORC1 (Saxton and Sabatini, 2017). It may also indicate increased phosphatase activity due to growth inhibition, which is supported by the enrichment of phosphorylated proteins carrying the GO term "phosphatase binding" (Figure 1E). To directly study changes in phosphatase activity due to culture conditions, we used the non-specific phosphatase substrate p-Nitrophenyl phosphate and could show that phosphatase enzymatic activity is increased by 30% in starvation compared to growth conditions (Figure S5). This increase seemed not to depend on functional autophagy, as ATG7 KO cells exhibited a similar response (Figure S5), indicating that upstream signaling events that regulate autophagy might also play a role in regulating activities of phosphatases (O'Prey et al., 2017). Whether ULK1 directly regulates phosphatases is largely unknown. Therefore, we screened the list of bona fide ULK1 targets identified in this study for catalytic and regulatory phosphatase subunits and could generate a network of 14 proteins, indicating that ULK1 directly regulates an elaborate phosphatase network, among them all three members of the striatin family of regulatory PP2A subunits, STRN, STRN3, and STRN4, as well as PP6 regulatory subunits (Figures 3F and 4A).

To address altered phosphoprotein phosphatase (PPP) activity due to increased ULK1 activity, we performed chemical proteomic experiments. Immobilized nonselective PPP inhibitor microcystin-LR was used in combination with differentially treated, SILAC-labeled cells to perform activity-based enrichments of PPP complexes (see STAR Methods for details). Briefly, microcystin-LR binds to the active site of catalytic subunits of

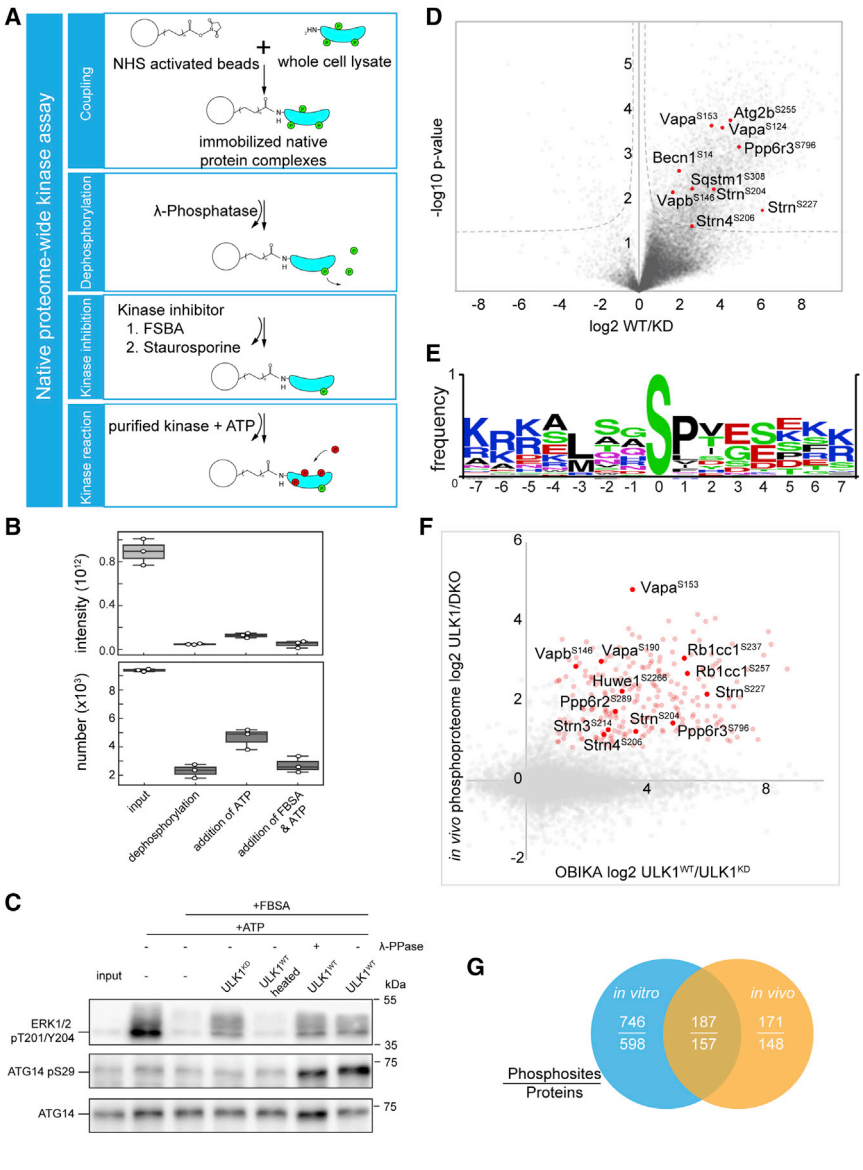

Figure 3. Proteome-wide, on-bead *in vitro* kinase assay (OBIKA) identifies bona fide ULK1 targets

(A) OBIKA workflow. After the indicated kinase reaction, samples were processed for bottom-up phosphoproteomic experiments as outlined in Figure 1A.

(B) Summed intensities and numbers of identified phosphosites highlight the effects of indicated steps within the OBIKA workflow. The addition of ATP leads to increased detection of phosphosites due to activity of endogenous kinases immobilized on NHS beads. Addition of the kinase inhibitor FBSA blunts this activity (box whisker plots; whiskers indicate largest and lowest points within 1.5 times of the interquartile range; n = 3). After each indicated step, three wash steps were performed prior to on-bead trypsin digestion, phosphopeptide enrichment, and analysis by LC-MS/MS.

(C) Proof of principle of OBIKA, analyzing known phosphosites by site-specific western blots. The MEK phosphosites on ERK1/2 were phosphorylated by endogenous, bead-bound MEK after the addition of ATP, which could be blocked by covalently inhibiting bead-bound MEK by FBSA. The ULK1 target site on ATG14, Ser29 was only phosphorylated after the addition of exogenous ULK1^{WT}. ULK1^{KD} or heat-inactivated ULK1^{WT} were used as negative controls. Cell lysate was generated using DKO MEFs.

(D) Significantly regulated phosphosites of ULK1 OBIKAs. Volcano plot comparing ULK1^{WT} (WT) with ULK1^{KD} (KD) OBIKAs (n = 3). Significantly regulated sites are marked with dashed lines (FDR < 0.05; BH-corrected). Sites marked in red are examples of proteins linked to autophagy as well as of phosphatase subunits identified in this study, including STRN.

(E) Motif analysis of *in vitro* ULK1 targets. Sites identified *in vitro* confirm the published ULK1 motif.

(F) New bona fide ULK1 sites identified *in vivo* and *in vitro*. Scatterplot highlights extent of regulation of newly identified ULK1 target sites identified by both *in vivo* and *in vitro* phosphoproteomic approaches. Significantly regulated sites in both approaches are marked in red (p < 0.05; BH-corrected).

(G) Comparison between *in vivo* and *in vitro* analyses. Venn diagram depicts the overlap of both approaches on site and protein level.

PPP (Goldberg et al., 1995), its binding being dependent on the abundance as well as on the accessibility, i.e., activity of the catalytic subunit (Lyons et al., 2018). Thus, based on altered enrichment levels, changes in PPP activity can be inferred. To test if microcystin-LR-based enrichments can indeed be used to deduce changes in phosphatase activity, we performed microcystin-LR-based enrichments in combination with increasing concentrations of okadaic acid, a rather specific PP2A inhibitor (Takai et al., 1992). Supporting the interpretation that enrichment levels reflect at least partial changes in activity, we could outcompete PP2A enrichment by okadaic acid, whereas we did not observe an effect on PP1 enrichments (Figure S5).

Comparing (1) starved ULK1 MEFs to starved DKO MEFs (Figure 4B; n = 3; Table S4) and (2) rapamycin-treated A549 cells to cells kept in full medium (Figure 4C; n = 3; Table S4), we observed genotype- and stimulus-dependent increased enrichments of PP2A and PP6 complexes, which both consist of catalytic, scaffold, and regulatory subunits (Shi, 2009). The increased enrichment of respective catalytic subunits indicated increased phosphatase activity under the examined conditions (Figures 4B and 4C). The observed differential enrichment of specific phosphatase regulatory subunits indicated altered complex compositions due to stress conditions. Interestingly, STRN, STRN3, and STRN4, as well as the regulatory PP6 subunits PPP6R2 and PPP6R3, which were already identified as carrying significantly regulated phosphosites within ULK1 kinase motifs, were enriched under autophagy-promoting conditions (Figures 4A–4C). The increased enrichment of STRN, STRN4, and PPP6R2 from rapamycin-treated A549 cells could also be shown by microcystin-LR-based activity purification coupled

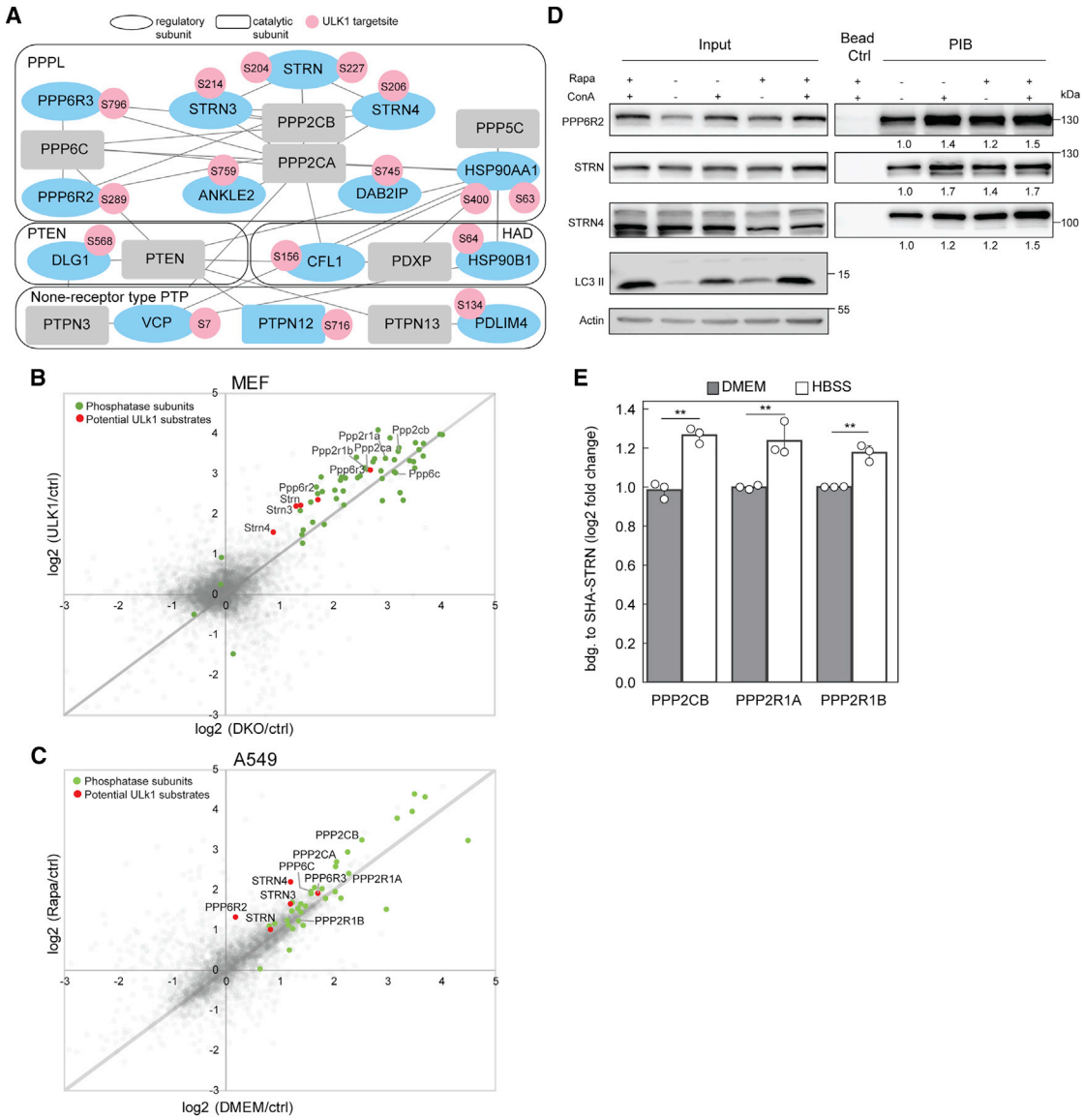

Figure 4. The ULK1-regulated phosphatase network

(A) Protein interaction network of phosphatase subunits that were identified as being direct ULK1 targets. A network of 14 phosphatase-interacting proteins that carry ULK1-regulated phosphosites was constructed using cytoscape according to data from STRING DB (Szklarczyk et al., 2019). Catalytic subunits not phosphorylated by ULK1 are marked in gray. Phosphosites are indicated as red circles. Boxes mark structural phosphatase families: PPPL, PPP-like fold phosphatases; PTP, protein tyrosine phosphatases; HAD, haloacid dehalogenase; PTEN, phosphatase and tensin homolog.

(B and C) Phosphatase-activity enrichment MS. Cells were treated as indicated, and phosphatases were enriched based on their activity using immobilized microcystin-LR. (B) shows MEFs and (C) shows A549 cells highlighting the increased enrichment of PP2 and PP6 subunits, among them all three striatin isoforms, STRN, STRN3, and STRN4 in mouse and human cells (each n = 3).

(D) Phosphatase-activity enrichment western blot. Proteins identified as enriched under autophagy inducing conditions in (B) and (C), reflecting higher phosphatase activity, were analyzed by immobilized microcystin-LR-based affinity purification (AP) coupled to western blots confirming MS experiments. MAP1LC3B-II (LC3 II) was used to highlight autophagy flux in the respective conditions, actin was used as loading control. Concanamycin A (ConA), an inhibitor of lysosomal V-ATPase, was used to inhibit lysosomal acidification and, by this, block protein degradation. Numbers indicate fold change as determined by densitometry. PIBs, phosphatase-inhibitor beads.

(E) Anti-SHA-STRN AP coupled to MS. In a reverse AP, ectopically expressed SHA-tagged STRN was enriched, and binding proteins were quantified compared to negative controls using cells not expressing SHA-STRN by label-free MS. Annotated PP2A subunits were significantly enriched (n = 3; $^{**}p < 0.01$; t test). Error bars indicate the 95% confidence interval. Note: STRN isoform 2 was used for all ectopic expression experiments.

CellPress
OPEN ACCESS

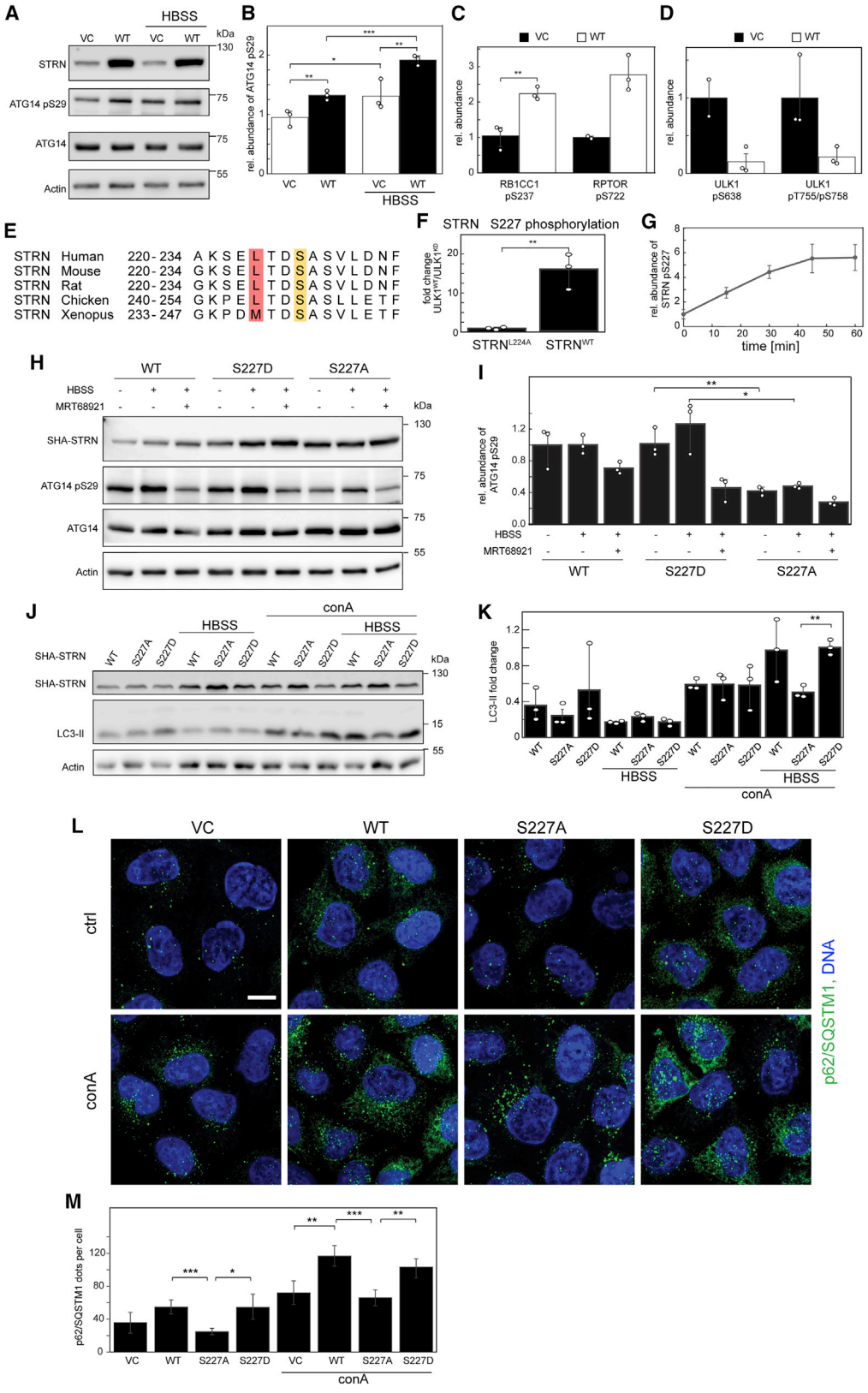

(legend on next page)

to western blot (Figure 4D). In a reversed setup by classical affinity purification-MS experiments, increased binding of PPP2CB, PPP2R1A, and R1B to SHA-tagged STRN was confirmed (Figure 4E; n = 3). Thus, induction of autophagy and increased ULK1 activity led to increased PP2A activity, which was accompanied by changes in PP2A protein-protein interactions, i.e., binding to striatin regulatory complex members.

STRN is a direct ULK1 target and its phosphorylation promotes autophagy

To test if changes in STRN abundance were coupled to ULK1 activity in a potential feedback mechanism, we ectopically expressed wild-type STRN ($STRN^{WT}$) in HeLa and Caco-2 cells and could indeed show that this led to cell-line-independent, increased ULK1 activity, as indicated by ATG14 Ser29 phosphorylation (Figures 5A and 5B; n = 3; Figure S6) (Klionsky et al., 2021). In agreement, we also identified increased abundance of ULK1 target sites on FIP200/RB1CC1 and RPTOR in cells ectopically expressing $STRN^{WT}$ (Figure 5C) (Gwinn et al., 2008; Mercer et al., 2021). In contrast, shRNA-based knockdown of STRN led to a reduction of ULK1 activity (Figure S6). The effect of STRN on ULK1 seemed to be direct via the PP2A holo-complex, as we detected a decreased abundance of inhibitory mTORC1 target sites on ULK1 in HeLa cells ectopically expressing STRN (Figure 5D) (Egan et al., 2011; Shang et al., 2011). mTORC1 activity itself seemed not be perturbed by changes in STRN abundance, as a respective target site on ribosomal protein S6 kinase RPS6KB1 was unresponsive (Figure S6) (Saitoh et al., 2002).

The identified ULK1 target site Ser227 on STRN is highly conserved within vertebrates, indicating physiological relevance (Figure 5E). To further prove that ULK1 is the kinase responsible for phosphorylating this site, we mutated leucin 224 within the ULK1 motif to alanine and repeated *in vitro* kinase assays using purified $STRN^{WT}$ and $STRN^{L224A}$ and comparing $ULK1^{WT}$ with $ULK1^{KD}$. Only the combination of $STRN^{WT}$ and $ULK1^{WT}$ gave rise to a significant increase in phosphorylation of Ser227, highlighting the importance of the kinase motif and supporting the interpretation that ULK1 directly phosphorylates this site *in vitro* and *in vivo* (Figure 5F). This was further supported by a time-dependent increase in phosphorylation over a period of 60 minutes *in vivo*, in agreement with a time-dependent increase of ULK1 activity in autophagy-inducing conditions (Figure 5G) (Rigbolt et al., 2014; Russell et al., 2013).

To study the functional consequences of ULK1 phosphorylation of STRN Ser227, we analyzed the effects of STRN site mutants on ULK1 and autophagy activity. ULK1 activity was again assessed by ATG14 Ser29 phosphorylation. Comparing ULK1 activity in cells expressing STRN mutants containing either a phosphomimetic aspartate residue or a non-phosphorylatable alanine residue instead of the characterized ULK1-dependent Ser227 phosphorylation site, we could show that alanine mutation led to a significant decrease in ULK1 activity (Figures 5H and 5I; n = 3). This was rescued by aspartate mutation. As a positive control, ATG14 phosphorylation was blocked by the ULK1-specific inhibitor MRT68921 (Petherick et al., 2015). Autophagy activity was assessed by analyzing the lipidation of MAP1LC3B (LC3-II), an autophagosomal marker protein important for autophagosome maturation and target recruitment, and by studying the turnover of p62/SQSTM1, the prototypic selective autophagy receptor (Johansen and Lamark, 2020), in the absence and presence of the lysosomal inhibitor concanamycin A (ConA). Both assays are a well-established proxy to analyze autophagy-dependent protein degradation within lysosomes, i.e.,

Figure 5. STRN is a direct ULK1 target

(A–D) Ectopic expression of STRN increases ULK1 activity. HeLa cells transfected with an empty control vector (VC) and cells ectopically expressing SHA-tagged $STRN^{WT}$ (WT) were analyzed on changes in ULK1 activity by monitoring: (A and B) the phosphorylation of Ser29 of ATG14 by phosphosite-specific western blots. Actin was used as loading control. (B) shows quantification of three biological replicates, and (C) shows the phosphorylation of indicated known ULK1 target sites by quantitative phosphoproteomics. XICs of respective phosphopeptides were used for quantification. Protein abundances were used for normalization; (D) the phosphorylation of known inhibitory mTORC1 target sites on ULK1 itself. Data were analyzed as in (C). In the case of Thr755 and Ser758 of ULK1, the phosphorylation site could not be unambiguously localized. Expression of STRN led to a significant increase of ULK1 activity. Error bars indicate the 95% confidence interval (*$p < 0.05$; **$p < 0.01$; t test). Note: STRN isoform 2 was used for all ectopic expression experiments.

(E) Conservation of amino acid sequences surrounding the ULK1 target site Ser227 on human STRN. The hydrophobic amino acid residues in −3 position to the ULK1 target sites are marked in red. Serine residues phosphorylated by ULK1 are highlighted in yellow.

(F) The ULK1 kinase motif is necessary for phosphorylation of $STRN^{Ser227}$ by ULK1. *In vitro* kinase assays performed with purified $ULK1^{WT}$, $ULK1^{KD}$, $STRN^{WT}$, and $STRN^{L224A}$ highlight the importance of the leucine residue at −3 (n = 3; **$p < 0.01$; t test). A respective alanine mutation significantly inhibited phosphorylation reactions. Respective phosphopeptides, i.e., $STRN^{222-235}$, were quantified by MS using XICs. Error bars indicate the 95% confidence interval.

(G) Time-dependent phosphorylation of STRN Ser227 under starvation conditions. A549 cells were starved for up to 60 minutes in HBSS, and STRN Ser227 phosphorylation was relatively quantified using a parallel-reaction monitoring (PRM) assay analyzing the respective tryptic peptide (n = 3). Error bars indicate standard deviations. All time points are significantly different from 0 minutes (t test; $p < 0.01$).

(H and I) Non-phosphorylatable STRN mutant inhibits ULK1 activity. ULK1 activity was monitored via the phosphorylation of Ser29 of ATG14. The non-phosphorylatable alanine mutation in STRN (S227A) reduces ULK1 activity, whereas the phosphomimicking aspartate mutation (S227D) restores WT levels. The ULK1 inhibitor MRT68921 was used as control. Actin was used as loading control. (A) shows respective vector control cells. (I) shows quantification of three biological replicates (*$p < 0.05$; **$p < 0.01$; t test). Error bars indicate the 95% confidence interval.

(J and K) Non-phosphorylatable STRN mutant blocks LC3 lipidation. Non-functional alanine mutation of the ULK1 target site Ser227 of STRN (S227A) significantly blocked autophagy flux under starvation conditions, as analyzed by LC3 lipidation (LC3-II). The phospho-mimicking aspartate mutation (S227D) rescued this phenotype. Actin was used as loading control. (A) shows respective vector control cells. (K) shows quantification of three biological replicates (**$p < 0.01$; t test). Error bars indicate the 95% confidence interval.

(L and M) Non-phosphorylatable STRN mutant blocks p62/SQSTM1 dot turnover. HeLa were either treated for 1 h with ConA (20 nM) or left untreated and stained for endogenous p62/SQSTM1. ConA treatment leads to an accumulation of immunostained protein. Scale bars, 10 μm. Representative confocal images are shown (L). Quantification of p62/SQSTM1 dots was done using ImageJ and Fiji ($n \geq 4$, M). *$p < 0.05$; **$p < 0.01$; ***$p < 0.001$; t test. Error bars indicate 95% confidence interval.

autophagy flux (Klionsky et al., 2021). In agreement to the observed effects on ULK1 activity, we could show that the alanine mutation led to a significant block in autophagy flux, which was rescued by the aspartate variant, as assayed by western blot following LC3 lipidation (Figures 5J and 5K; n = 3) and by immunofluorescence imaging studying the p62/SQSTM1 dot formation (Figures 5L and 5M). Thus, ULK1 and PP2A-STRN are linked in a positive feedback loop, the phosphorylation of STRN Ser227 by ULK1 being critical for ULK1 activity and protein degradation by autophagy.

DISCUSSION

Autophagy is a vital, evolutionarily conserved catabolic process; its robust regulation is a prerequisite for proper cell homeostasis (Mizushima and Levine, 2020). Vital cellular pathways are controlled by robust signaling systems, which are characterized by multilayered regulatory circuits including feedback loops, ensuring that only stimuli of the appropriate strength and duration are capable to turn the respective responses on or off (Azeloglu and Iyengar, 2015). In the present study, we uncovered numerous ULK1 target proteins known to be important for autophagy regulation, underlining its multilayered signaling input affecting all steps of autophagosome biogenesis and turnover. In addition, a positive feedback loop between ULK1 and the PP2A complex was studied, characterizing the regulatory subunit STRN as a bona fide ULK1 target being critical for proper ULK1 and with this autophagy activation.

To identify and quantify phosphorylation-based signaling events, MS-based phosphoproteomic approaches are the method of choice (Aebersold and Mann, 2016). However, despite enormous technical and bioinformatical progress in phosphosite mapping and scoring (Ochoa et al., 2020), we still try to establish comprehensive phosphosite repositories and are far from understanding their biological significance on a global scale. More than 95% of reported human phosphosites have no known biological function or responsible kinase (Needham et al., 2019). Knowledge of kinase-substrate relations is not just of basic interest but has direct translational implications, e.g., in kinase-inhibitor-based cancer therapies. Knowledge of all substrates of a specific kinase would allow a more efficient prediction of potential adverse effects of respective kinase inhibitors (Braun et al., 2020). Kinase-substrate relationships have been studied by *in vivo* as well as *in vitro* approaches (Arrington et al., 2019; von Stechow et al., 2015; Wang et al., 2020). The discrimination of direct and indirect kinase effects *in vivo*, however, is challenging. Therefore, the gold standard to biochemically prove direct kinase-substrate relationships are *in vitro* kinase assays, in which purified kinase and substrate are incubated and phosphorylation reactions are analyzed. One shortcoming of these approaches is the identification of false-positive sites due to a lack of substrate competition. To address this, different variants of *in vitro* kinase assays were developed in which more complex samples, such as peptide libraries or denatured protein mixtures, were used (Kubota et al., 2009; Xue et al., 2014). Still, the usage of peptides or denaturing conditions, which interfere with tertiary/quaternary protein structures important for kinase-substrate interaction, raise questions on the *in vivo* relevance of such assays.

Here, we introduced an OBIKA that addresses these shortcomings by using an immobilized cell proteome under native conditions as input for *in vitro* kinase reactions, in which endogenous kinases are permanently inhibited. As proof of concept, we studied ULK1 signaling and its role in regulating protein degradation by autophagy. By combining *in vivo* and *in vitro* phosphoproteomic datasets, we identified 187 bona fide ULK1 target sites, which more than triples the number of known ULK1 target sites according to www.phosphosite.org. As is commonly the case for phosphoproteomic studies, the overlap between the dataset of this study with other recently published ULK1 datasets is rather small (Mercer et al., 2018, 2021), which is likely due to the differently used cell models, experimental approaches, and noise of these studies. This also indicates that the actual number of phosphorylation events is likely significantly higher than reported in the respective studies. Although we cannot exclude a systematic bias of OBIKA leading to the identification of false-positive sites, as indicated by the higher number of potential ULK1 target sites compared to *in vivo* analyses, we are confident that the presented method highlights a significant improvement compared to current approaches. Combining *in vitro* analyses with pharmacological inhibition of WT kinases *in vitro* as well as *in vivo* might further help in shortlisting true kinase targets. The underlying principle of the *in vitro* assay should also be applicable to study other posttranslational modifications, such as acetylation and ubiquitination, with the only prerequisite being the availability of covalent inhibitors of enzymes catalyzing the respective reactions.

Interestingly, ULK1 appeared to directly regulate an entire phosphatase network, including PP2A, PP5, and PP6 Ser/Thr phosphatase complexes. Also, protein-tyrosine phosphatases were characterized as direct ULK1 targets. Phosphotyrosine-based signaling is supposed to happen upstream of ULK1, indicating a potential feedback of ULK1 to signal transducers at the plasma membrane. The heterotrimeric PP2A complex, consisting of the catalytic subunit PPP2CA, the scaffolding subunit PPP2R1B/PRL65, and the regulatory subunit PPP2R5A/B55alpha, was shown to be critical for ULK1 dephosphorylation under starvation conditions (Wong et al., 2015). We characterized the regulatory PP2A subunit STRN as a direct ULK1 target and showed increased interaction of STRN, PPP2R1A/1B, and PPP2CB under autophagy-inducing conditions. Striatins are also members of the evolutionarily conserved STRIPAK complexes, which link PP2A complexes with germinal center kinases (Kück et al., 2019) including STK26/MST4, which was recently shown to activate autophagy via phosphorylation of ATG4B (Huang et al., 2017). In addition, striatins were shown to transform anti-tumorigenic into pro-tumorigenic PP2A complexes by interfering with the tumor suppressor Hippo pathway, which was shown to crosstalk with autophagy, e.g., via AMP-activated protein kinase, affecting tumor progression in a context-dependent manner (Kim et al., 2020; Tang and Christofori, 2020; Tang et al., 2020). Thus, it appears that several distinct PP2A complexes are involved in autophagy regulation, ULK1 potentially affecting PP2A complex architecture and, with this, the PP2A substrate repertoire and/or subcellular localization. Striatins appear to function as important scaffolds, linking autophagy signal transduction to several other cellular pathways, by

supporting, among others, the direct dephosphorylation, i.e., activation of ULK1 by PP2A.

Taken together, we developed a proteome-wide *in vitro* kinase assay with which kinase substrates under native conditions can be screened in a highly multiplexed manner and used it to study the crosstalk between ULK1 kinase and PP2A phosphatase complexes. By studying autophagy signaling, we identified kinase-phosphatase networks and highlighted the function of one kinase-phosphatase feedback mechanism on protein degradation. Our data imply the existence of additional highly sophisticated kinase-phosphatase feedback mechanisms being critical for the robust regulation of protein turnover by autophagy.

STAR★METHODS

Detailed methods are provided in the online version of this paper and include the following:

- KEY RESOURCES TABLE
- RESOURCE AVAILABILITY
  - Lead contact
  - Materials availability
  - Data and code availability
- EXPERIMENTAL MODEL AND SUBJECT DETAILS
- METHOD DETAILS
  - Recombinant DNA constructs and virus production
  - ULK1 and ULK1^{D165A} protein purification
  - Cell culture and treatments
  - Cell lysis
  - Immunoblotting
  - Immunostainings and fluorescence microscopy
  - Affinity purification
  - PPPome activity enrichment
  - *In vitro* kinase assay
  - Protein digestion and sample preparation for MS
  - PRM assays
  - LC-MS/MS analyses
- QUANTIFICATION AND STATISTICAL ANALYSES

SUPPLEMENTAL INFORMATION

Supplemental information can be found online at https://doi.org/10.1016/j.celrep.2021.109762.

ACKNOWLEDGMENTS

This research was supported by the University of Fribourg and the Swiss National Science Foundation (J.D.) and was part of the SKINTEGRITY.CH collaborative research project. We thank Dieter Kressler for technical support and intellectual input and Valentia Cianfanelli for critically discussing the data and helpful suggestions.

AUTHOR CONTRIBUTIONS

Conceptualization, Z.H and J.D.; methodology, Z.H., D.S.S., and J.D.; investigation, Z.H., D.S.S., B.V., A.L., C.V., W.W., M.S., and E.M.-M.; writing – original draft, Z.H. and J.D.; writing – review & editing, B.S. and J.D.; funding acquisition, resources, and supervision, B.S. and J.D.

DECLARATION OF INTEREST

The authors declare no competing interests.

Received: January 28, 2021
Revised: July 16, 2021
Accepted: September 6, 2021
Published: September 28, 2021

REFERENCES

Aebersold, R., and Mann, M. (2016). Mass-spectrometric exploration of proteome structure and function. Nature *537*, 347–355.

Arrington, J., Xue, L., Wang, W.H., Geahlen, R.L., and Tao, W.A. (2019). Identification of the Direct Substrates of the ABL Kinase via Kinase Assay Linked Phosphoproteomics with Multiple Drug Treatments. J. Proteome Res. *18*, 1679–1690.

Azeloglu, E.U., and Iyengar, R. (2015). Signaling networks: information flow, computation, and decision making. Cold Spring Harb. Perspect. Biol. *7*, a005934.

Bakula, D., Müller, A.J., Zuleger, T., Takacs, Z., Franz-Wachtel, M., Thost, A.-K., Brigger, D., Tschan, M.P., Frickey, T., Robenek, H., et al. (2017). WIPI3 and WIPI4 β-propellers are scaffolds for LKB1-AMPK-TSC signalling circuits in the control of autophagy. Nat. Commun. *8*, 15637.

Bar-Peled, L., Schweitzer, L.D., Zoncu, R., and Sabatini, D.M. (2012). Ragulator is a GEF for the rag GTPases that signal amino acid levels to mTORC1. Cell *150*, 1196–1208.

Barz, S., Kriegenburg, F., Henning, A., Bhattacharya, A., Mancilla, H., Sánchez-Martín, P., and Kraft, C. (2020). Atg1 kinase regulates autophagosome-vacuole fusion by controlling SNARE bundling. EMBO Rep. *21*, e51869.

Batth, T.S., Francavilla, C., and Olsen, J.V. (2014). Off-line high-pH reversed-phase fractionation for in-depth phosphoproteomics. J. Proteome Res. *13*, 6176–6186.

Bhutia, S.K., Kegelman, T.P., Das, S.K., Azab, B., Su, Z.Z., Lee, S.G., Sarkar, D., and Fisher, P.B. (2010). Astrocyte elevated gene-1 induces protective autophagy. Proc. Natl. Acad. Sci. USA *107*, 22243–22248.

Bindea, G., Mlecnik, B., Hackl, H., Charoentong, P., Tosolini, M., Kirilovsky, A., Fridman, W.H., Pagès, F., Trajanoski, Z., and Galon, J. (2009). ClueGO: a Cytoscape plug-in to decipher functionally grouped gene ontology and pathway annotation networks. Bioinformatics *25*, 1091–1093.

Braun, T.P., Eide, C.A., and Druker, B.J. (2020). Response and Resistance to BCR-ABL1-Targeted Therapies. Cancer Cell *37*, 530–542.

Chan, E.Y., and Tooze, S.A. (2009). Evolution of Atg1 function and regulation. Autophagy *5*, 758–765.

Chan, E.Y., Kir, S., and Tooze, S.A. (2007). siRNA screening of the kinome identifies ULK1 as a multidomain modulator of autophagy. J. Biol. Chem. *282*, 25464–25474.

Cox, J., and Mann, M. (2008). MaxQuant enables high peptide identification rates, individualized p.p.b.-range mass accuracies and proteome-wide protein quantification. Nat. Biotechnol. *26*, 1367–1372.

Di Bartolomeo, S., Corazzari, M., Nazio, F., Oliverio, S., Lisi, G., Antonioli, M., Pagliarini, V., Matteoni, S., Fuoco, C., Giunta, L., et al. (2010). The dynamic interaction of AMBRA1 with the dynein motor complex regulates mammalian autophagy. J. Cell Biol. *191*, 155–168.

Di Rita, A., Peschiaroli, A., Acunzo, P.D., Strobbe, D., Hu, Z., Gruber, J., Nygaard, M., Lambrughi, M., Melino, G., Papaleo, E., et al. (2018). HUWE1 E3 ligase promotes PINK1/PARKIN-independent mitophagy by regulating AMBRA1 activation via IKKα. Nat. Commun. *9*, 3755.

Dikic, I., and Elazar, Z. (2018). Mechanism and medical implications of mammalian autophagy. Nat. Rev. Mol. Cell Biol. *19*, 349–364.

Egan, D.F., Shackelford, D.B., Mihaylova, M.M., Gelino, S., Kohnz, R.A., Mair, W., Vasquez, D.S., Joshi, A., Gwinn, D.M., Taylor, R., et al. (2011).

Phosphorylation of ULK1 (hATG1) by AMP-activated protein kinase connects energy sensing to mitophagy. Science *331*, 456–461.

Egan, D.F., Chun, M.G., Vamos, M., Zou, H., Rong, J., Miller, C.J., Lou, H.J., Raveendra-Panickar, D., Yang, C.C., Sheffler, D.J., et al. (2015). Small Molecule Inhibition of the Autophagy Kinase ULK1 and Identification of ULK1 Substrates. Mol. Cell *59*, 285–297.

Ganley, I.G., Lam, D.H., Wang, J., Ding, X., Chen, S., and Jiang, X. (2009). ULK1.ATG13.FIP200 complex mediates mTOR signaling and is essential for autophagy. J. Biol. Chem. *284*, 12297–12305.

Gao, J., Kurre, R., Rose, J., Walter, S., Fröhlich, F., Piehler, J., Reggiori, F., and Ungermann, C. (2020). Function of the SNARE Ykt6 on autophagosomes requires the Dsl1 complex and the Atg1 kinase complex. EMBO Rep. *21*, e50733.

Goldberg, J., Huang, H.B., Kwon, Y.G., Greengard, P., Nairn, A.C., and Kuriyan, J. (1995). Three-dimensional structure of the catalytic subunit of protein serine/threonine phosphatase-1. Nature *376*, 745–753.

Gwinn, D.M., Shackelford, D.B., Egan, D.F., Mihaylova, M.M., Mery, A., Vasquez, D.S., Turk, B.E., and Shaw, R.J. (2008). AMPK phosphorylation of raptor mediates a metabolic checkpoint. Mol. Cell *30*, 214–226.

Hosokawa, N., Hara, T., Kaizuka, T., Kishi, C., Takamura, A., Miura, Y., Iemura, S., Natsume, T., Takehana, K., Yamada, N., et al. (2009). Nutrient-dependent mTORC1 association with the ULK1-Atg13-FIP200 complex required for autophagy. Mol. Biol. Cell *20*, 1981–1991.

Hu, Z., Raucci, S., Jaquenoud, M., Hatakeyama, R., Stumpe, M., Rohr, R., Reggiori, F., De Virgilio, C., and Dengjel, J. (2019). Multilayered Control of Protein Turnover by TORC1 and Atg1. Cell Rep. *28*, 3486–3496.e6.

Huang, T., Kim, C.K., Alvarez, A.A., Pangeni, R.P., Wan, X., Song, X., Shi, T., Yang, Y., Sastry, N., Horbinski, C.M., et al. (2017). MST4 Phosphorylation of ATG4B Regulates Autophagic Activity, Tumorigenicity, and Radioresistance in Glioblastoma. Cancer Cell *32*, 840–855.e8.

Johansen, T., and Lamark, T. (2020). Selective Autophagy: ATG8 Family Proteins, LIR Motifs and Cargo Receptors. J. Mol. Biol. *432*, 80–103.

Jung, C.H., Jun, C.B., Ro, S.H., Kim, Y.M., Otto, N.M., Cao, J., Kundu, M., and Kim, D.H. (2009). ULK-Atg13-FIP200 complexes mediate mTOR signaling to the autophagy machinery. Mol. Biol. Cell *20*, 1992–2003.

Kim, J., Kundu, M., Viollet, B., and Guan, K.L. (2011). AMPK and mTOR regulate autophagy through direct phosphorylation of Ulk1. Nat. Cell Biol. *13*, 132–141.

Kim, J.W., Berrios, C., Kim, M., Schade, A.E., Adelmant, G., Yeerna, H., Damato, E., Iniguez, A.B., Florens, L., Washburn, M.P., et al. (2020). STRIPAK directs PP2A activity toward MAP4K4 to promote oncogenic transformation of human cells. eLife *9*, e53003.

Klionsky, D.J., Abdel-Aziz, A.K., Abdelfatah, S., Abdellatif, M., Abdoli, A., Abel, S., Abeliovich, H., Abildgaard, M.H., Abudu, Y.P., Acevedo-Arozena, A., et al. (2021). Guidelines for the use and interpretation of assays for monitoring autophagy (4th edition). Autophagy *17*, 1–382.

Kubota, K., Anjum, R., Yu, Y., Kunz, R.C., Andersen, J.N., Kraus, M., Keilhack, H., Nagashima, K., Krauss, S., Paweletz, C., et al. (2009). Sensitive multiplexed analysis of kinase activities and activity-based kinase identification. Nat. Biotechnol. *27*, 933–940.

Kück, U., Radchenko, D., and Teichert, I. (2019). STRIPAK, a highly conserved signaling complex, controls multiple eukaryotic cellular and developmental processes and is linked with human diseases. Biol. Chem. Published online May 1, 2019. https://doi.org/10.1515/hsz-2019-0173.

Löffler, A.S., Alers, S., Dieterle, A.M., Keppeler, H., Franz-Wachtel, M., Kundu, M., Campbell, D.G., Wesselborg, S., Alessi, D.R., and Stork, B. (2011). Ulk1-mediated phosphorylation of AMPK constitutes a negative regulatory feedback loop. Autophagy *7*, 696–706.

Lyons, S.P., Jenkins, N.P., Nasa, I., Choy, M.S., Adamo, M.E., Page, R., Peti, W., Moorhead, G.B., and Kettenbach, A.N. (2018). A Quantitative Chemical Proteomic Strategy for Profiling Phosphoprotein Phosphatases from Yeast to Humans. Mol. Cell. Proteomics *17*, 2448–2461.

MacLean, B., Tomazela, D.M., Shulman, N., Chambers, M., Finney, G.L., Frewen, B., Kern, R., Tabb, D.L., Liebler, D.C., and MacCoss, M.J. (2010). Skyline: an open source document editor for creating and analyzing targeted proteomics experiments. Bioinformatics *26*, 966–968.

Madeira, F., Park, Y.M., Lee, J., Buso, N., Gur, T., Madhusoodanan, N., Basutkar, P., Tivey, A.R.N., Potter, S.C., Finn, R.D., and Lopez, R. (2019). The EMBL-EBI search and sequence analysis tools APIs in 2019. Nucleic Acids Res. *47* (*W1*), W636–W641.

McAlpine, F., Williamson, L.E., Tooze, S.A., and Chan, E.Y. (2013). Regulation of nutrient-sensitive autophagy by uncoordinated 51-like kinases 1 and 2. Autophagy *9*, 361–373.

Mercer, T.J., Gubas, A., and Tooze, S.A. (2018). A molecular perspective of mammalian autophagosome biogenesis. J. Biol. Chem. *293*, 5386–5395.

Mercer, T.J., Ohashi, Y., Boeing, S., Jefferies, H.B.J., De Tito, S., Flynn, H., Tremel, S., Zhang, W., Wirth, M., Frith, D., et al. (2021). Phosphoproteomic identification of ULK substrates reveals VPS15-dependent ULK/VPS34 interplay in the regulation of autophagy. EMBO J. *40*, e105985.

Mintern, J.D., and Villadangos, J.A. (2012). Autophagy and mechanisms of effective immunity. Front. Immunol. *3*, 60.

Mizushima, N., and Levine, B. (2020). Autophagy in Human Diseases. N. Engl. J. Med. *383*, 1564–1576.

Nakatogawa, H. (2020). Mechanisms governing autophagosome biogenesis. Nat. Rev. Mol. Cell Biol. *21*, 439–458.

Needham, E.J., Parker, B.L., Burykin, T., James, D.E., and Humphrey, S.J. (2019). Illuminating the dark phosphoproteome. Sci. Signal. *12*, eaau8645.

Nettling, M., Treutler, H., Grau, J., Keilwagen, J., Posch, S., and Grosse, I. (2015). DiffLogo: a comparative visualization of sequence motifs. BMC Bioinformatics *16*, 387.

Nthiga, T.M., Kumar Shrestha, B., Sjøttem, E., Bruun, J.A., Bowitz Larsen, K., Bhujabal, Z., Lamark, T., and Johansen, T. (2020). CALCOCO1 acts with VAMP-associated proteins to mediate ER-phagy. EMBO J. *39*, e103649.

O'Prey, J., Sakamaki, J., Baudot, A.D., New, M., Van Acker, T., Tooze, S.A., Long, J.S., and Ryan, K.M. (2017). Application of CRISPR/Cas9 to Autophagy Research. Methods Enzymol. *588*, 79–108.

Ochoa, D., Jarnuczak, A.F., Viéitez, C., Gehre, M., Soucheray, M., Mateus, A., Kleefeldt, A.A., Hill, A., Garcia-Alonso, L., Stein, F., et al. (2020). The functional landscape of the human phosphoproteome. Nat. Biotechnol. *38*, 365–373.

Park, J.M., Jung, C.H., Seo, M., Otto, N.M., Grunwald, D., Kim, K.H., Moriarity, B., Kim, Y.M., Starker, C., Nho, R.S., et al. (2016). The ULK1 complex mediates MTORC1 signaling to the autophagy initiation machinery via binding and phosphorylating ATG14. Autophagy *12*, 547–564.

Perez-Riverol, Y., Csordas, A., Bai, J., Bernal-Llinares, M., Hewapathirana, S., Kundu, D.J., Inuganti, A., Griss, J., Mayer, G., Eisenacher, M., et al. (2019). The PRIDE database and related tools and resources in 2019: improving support for quantification data. Nucleic Acids Res. *47* (*D1*), D442–D450.

Petherick, K.J., Conway, O.J., Mpamhanga, C., Osborne, S.A., Kamal, A., Saxty, B., and Ganley, I.G. (2015). Pharmacological inhibition of ULK1 kinase blocks mammalian target of rapamycin (mTOR)-dependent autophagy. J. Biol. Chem. *290*, 11376–11383.

Pyo, K.E., Kim, C.R., Lee, M., Kim, J.S., Kim, K.I., and Baek, S.H. (2018). ULK1 O-GlcNAcylation Is Crucial for Activating VPS34 via ATG14L during Autophagy Initiation. Cell Rep. *25*, 2878–2890.e4.

Rigbolt, K.T., Zarei, M., Sprenger, A., Becker, A.C., Diedrich, B., Huang, X., Eiselein, S., Kristensen, A.R., Gretzmeier, C., Andersen, J.S., et al. (2014). Characterization of early autophagy signaling by quantitative phosphoproteomics. Autophagy *10*, 356–371.

Russell, R.C., Tian, Y., Yuan, H., Park, H.W., Chang, Y.Y., Kim, J., Kim, H., Neufeld, T.P., Dillin, A., and Guan, K.L. (2013). ULK1 induces autophagy by phosphorylating Beclin-1 and activating VPS34 lipid kinase. Nat. Cell Biol. *15*, 741–750.

Saitoh, M., Pullen, N., Brennan, P., Cantrell, D., Dennis, P.B., and Thomas, G. (2002). Regulation of an activated S6 kinase 1 variant reveals a novel

mammalian target of rapamycin phosphorylation site. J. Biol. Chem. *277*, 20104–20112.

Saxton, R.A., and Sabatini, D.M. (2017). mTOR Signaling in Growth, Metabolism, and Disease. Cell *168*, 960–976.

Shang, L., Chen, S., Du, F., Li, S., Zhao, L., and Wang, X. (2011). Nutrient starvation elicits an acute autophagic response mediated by Ulk1 dephosphorylation and its subsequent dissociation from AMPK. Proc. Natl. Acad. Sci. USA *108*, 4788–4793.

Shannon, P., Markiel, A., Ozier, O., Baliga, N.S., Wang, J.T., Ramage, D., Amin, N., Schwikowski, B., and Ideker, T. (2003). Cytoscape: a software environment for integrated models of biomolecular interaction networks. Genome Res. *13*, 2498–2504.

Shi, Y. (2009). Serine/threonine phosphatases: mechanism through structure. Cell *139*, 468–484.

Siva Sankar, D., and Dengjel, J. (2020). Protein complexes and neighborhoods driving autophagy. Autophagy, Published online November 13, 2020. https://doi.org/10.1080/15548627.2020.1847461.

Szklarczyk, D., Gable, A.L., Lyon, D., Junge, A., Wyder, S., Huerta-Cepas, J., Simonovic, M., Doncheva, N.T., Morris, J.H., Bork, P., et al. (2019). STRING v11: protein-protein association networks with increased coverage, supporting functional discovery in genome-wide experimental datasets. Nucleic Acids Res. *47* (*D1*), D607–D613.

Takai, A., Murata, M., Torigoe, K., Isobe, M., Mieskes, G., and Yasumoto, T. (1992). Inhibitory effect of okadaic acid derivatives on protein phosphatases. A study on structure-affinity relationship. Biochem. J. *284*, 539–544.

Tang, F., and Christofori, G. (2020). The cross-talk between the Hippo signaling pathway and autophagy:implications on physiology and cancer. Cell Cycle *19*, 2563–2572.

Tang, Y., Fang, G., Guo, F., Zhang, H., Chen, X., An, L., Chen, M., Zhou, L., Wang, W., Ye, T., et al. (2020). Selective Inhibition of STRN3-Containing PP2A Phosphatase Restores Hippo Tumor-Suppressor Activity in Gastric Cancer. Cancer Cell *38*, 115–128.e9.

Thoresen, S.B., Pedersen, N.M., Liestøl, K., and Stenmark, H. (2010). A phosphatidylinositol 3-kinase class III sub-complex containing VPS15, VPS34, Beclin 1, UVRAG and BIF-1 regulates cytokinesis and degradative endocytic traffic. Exp. Cell Res. *316*, 3368–3378.

Torii, S., Yoshida, T., Arakawa, S., Honda, S., Nakanishi, A., and Shimizu, S. (2016). Identification of PPM1D as an essential Ulk1 phosphatase for genotoxic stress-induced autophagy. EMBO Rep. *17*, 1552–1564.

Tyanova, S., Temu, T., and Cox, J. (2016). The MaxQuant computational platform for mass spectrometry-based shotgun proteomics. Nat. Protoc. *11*, 2301–2319.

Valverde, D.P., Yu, S., Boggavarapu, V., Kumar, N., Lees, J.A., Walz, T., Reinisch, K.M., and Melia, T.J. (2019). ATG2 transports lipids to promote autophagosome biogenesis. J. Cell Biol. *218*, 1787–1798.

von Stechow, L., Francavilla, C., and Olsen, J.V. (2015). Recent findings and technological advances in phosphoproteomics for cells and tissues. Expert Rev. Proteomics *12*, 469–487.

Wang, P., Hsu, C.C., Du, Y., Zhu, P., Zhao, C., Fu, X., Zhang, C., Paez, J.S., Macho, A.P., Tao, W.A., and Zhu, J.K. (2020). Mapping proteome-wide targets of protein kinases in plant stress responses. Proc. Natl. Acad. Sci. USA *117*, 3270–3280.

Wiederschain, D., Wee, S., Chen, L., Loo, A., Yang, G., Huang, A., Chen, Y., Caponigro, G., Yao, Y.M., Lengauer, C., et al. (2009). Single-vector inducible lentiviral RNAi system for oncology target validation. Cell Cycle *8*, 498–504.

Wiśniewski, J.R., Zougman, A., Nagaraj, N., and Mann, M. (2009). Universal sample preparation method for proteome analysis. Nat. Methods *6*, 359–362.

Wold, M.S., Lim, J., Lachance, V., Deng, Z., and Yue, Z. (2016). ULK1-mediated phosphorylation of ATG14 promotes autophagy and is impaired in Huntington's disease models. Mol. Neurodegener. *11*, 76.

Wong, P.M., Feng, Y., Wang, J., Shi, R., and Jiang, X. (2015). Regulation of autophagy by coordinated action of mTORC1 and protein phosphatase 2A. Nat. Commun. *6*, 8048.

Wu, W., Wang, X., Berleth, N., Deitersen, J., Wallot-Hieke, N., Böhler, P., Schlütermann, D., Stuhldreier, F., Cox, J., Schmitz, K., et al. (2020). The Autophagy-Initiating Kinase ULK1 Controls RIPK1-Mediated Cell Death. Cell Rep. *31*, 107547.

Xue, L., Wang, P., Cao, P., Zhu, J.K., and Tao, W.A. (2014). Identification of extracellular signal-regulated kinase 1 (ERK1) direct substrates using stable isotope labeled kinase assay-linked phosphoproteomics. Mol. Cell. Proteomics *13*, 3199–3210.

Zachari, M., and Ganley, I.G. (2017). The mammalian ULK1 complex and autophagy initiation. Essays Biochem. *61*, 585–596.

Zarei, M., Sprenger, A., Rackiewicz, M., and Dengjel, J. (2016). Fast and easy phosphopeptide fractionation by combinatorial ERLIC-SCX solid-phase extraction for in-depth phosphoproteome analysis. Nat. Protoc. *11*, 37–45.

Zhao, Y.G., Liu, N., Miao, G., Chen, Y., Zhao, H., and Zhang, H. (2018). The ER Contact Proteins VAPA/B Interact with Multiple Autophagy Proteins to Modulate Autophagosome Biogenesis. Curr. Biol. *28*, 1234–1245.e4.

CellPress
OPEN ACCESS

STAR★METHODS

KEY RESOURCES TABLE

REAGENT or RESOURCE	SOURCE	IDENTIFIER
Antibodies		
Mouse monoclonal anti-PPP6R2	Santa Cruz Biotechnology	Cat#sc-376238; RRID:AB_10986121
Mouse monoclonalanti-STRN	Santa Cruz Biotechnology	Cat#sc-136084; RRID:AB_2271282
Rabbit polyclonal anti-STRN4	MERCK	Cat#SAB1302464
Rabbit polyclonal anti-LC3A/B	Cell Signaling Technology	Cat#4108S; RRID:AB_2137703
Rabbit monoclonal anti-ATG14-pS29	Cell Signaling Technology	Cat#92340S; RRID:AB_2800182
Rabbit monoclonal anti-ATG14	Cell Signaling Technology	Cat#96752; RRID:AB_2737056
Rabbit polyclonal anti-RPS6KB1-pT389	Cell Signaling Technology	Cat#9205; RRID:AB_330944
Rabbit polyclonal anti-ERK1/2-pT201/Y204	Cell Signaling Technology	Cat#9101S; RRID:AB_331646
Mouse monoclonal anti-β-Actin	Santa Cruz Biotechnology	Cat#sc-47778; RRID:AB_2714189
Peroxidase-conjugated goat anti-rabbit IgG	Jackson Immuno Research	Cat#111-035-045; RRID:AB_2337938
Peroxidase-conjugated goat anti-mouse IgG	Jackson Immuno Research	Cat#115-035-062; RRID:AB_2338504
guinea pig anti-SQSTM1	Progen	Cat#GP62-C; RRID:AB_2687531
anti-guinea pig	Invitrogen	Cat#A11073; RRID:AB_2534117
Bacterial and virus strains		
E. coli DH5α	CGSC	Cat#12384
Chemicals, peptides, and recombinant proteins		
DMEM	PAN Biotech	Cat#P04-04510
SILAC-DMEM	PAN Biotech	Cat#P04-02505
DPBS	PAN Biotech	Cat#P04-36500
HBSS	GIBCO	Cat#14025100
FBS	Biowest	Cat#S181B-500
Dialyzed FBS	Biowest	Cat#S181D-500
Penicillin/streptomycin	PAN Biotech	Cat#P06-07100
GlutaMAX	GIBCO	Cat#35050038
Trypsin for cell culture	PAN Biotech	Cat#P10-023100
Pierce Anti-HA Magnetic Beads	Thermo Scientific	Cat#88837
Strep-Tactin®XT 4Flow®	IBA	Cat#2-5030-010
Nitrocellulose membrane 0.45 μm	Amersham	Cat#GE10600000
PVDF membrane 0.2 μm	Amersham	Cat#GE10600021
TransBlot Turbo RTA Midi NC	BIO-RAD	Cat#1704271
TransBlot Turbo RTA Midi PVDF	BIO-RAD	Cat#1704273
WesternBright ECL	Advansta	Cat#K12049-D50
Benzonase	Sigma-Aldrich	Cat#1.01697.0001
Arg10	Sigma-Aldrich	Cat#608033
Arg6	Sigma-Aldrich	Cat#643440
Lys4	Sigma-Aldrich	Cat#616192
Lys8	Sigma-Aldrich	Cat#608041
Arg0	Sigma-Aldrich	Cat#11039
Lys0	Sigma-Aldrich	Cat#L8662
L-Proline	Fluka	Cat#81710
PhosSTOP	Roche	Cat#04-906-837-001
Proteases Inhibitor Cocktail	Roch	Cat#11-697-498-001
Rapamycin	LC Laboratories	Cat#R-5000

(*Continued on next page*)

Continued

REAGENT or RESOURCE	SOURCE	IDENTIFIER
Concanamycin A (conA)	Santa Cruz	Cat#sc-202111A
Microcystin-LR	Enzo Life Sciences	Cat#ALX-350-012-M001
5′-(4-Fluorosulfonylbenzoyl) adenosine hydrochloride (FSBA)	Sigma-Aldrich	Cat#F9128
Staurosporine	LC Laboratories	Cat#S-9300
MRT68921	Selleck	Cat#S7949
NHS-activated Sepharose 4 fast flow	GE Healthcare	Cat#17-0906-01
Trifluoroacetic acid (TFA)	Sigma-Aldrich	Cat#302031
Formic acid (FA)	Merck	Cat#5.43804.0250
Ammonia solution 25%	Merck	Cat#5438300250
Titanium dioxide (TiO2)	GL Sciences	Cat#5020-75010
Trypsin	Promega	Cat#V5113
γ-[$^{18}O_4$]-ATP	Cambridge Isotope Laboratories	Cat#OLM-7858-20
ATP	Sigma-Aldrich	Cat#A6419
Vivacon 500, 10'000 MWCO HYDROSART	Sartorius	Cat#VN01H02
C8 disc	3M Empore	Cat#14-386
C18 disc	3M Empore	Cat#14-386-2
Lys-C	FUJIFILM Wako Pure Chemical Corporation	Cat#129-02541
HR-X Column	Macherey-Nagel	Cat#730936P45
C18 Cartridges	Macherey-Nagel	Cat#731802
MS-grade Water	VWR	Cat#23595.328
MS-grade Acetonitrile	VWR	Cat#20060.32
C18 Column for High pH Fractionation	Waters	Cat#186003034
Pierce Anti-HA Magnetic Beads	Thermo Scientific	Cat#88837
Lambda Protein Phosphatase	NEB	Cat#P0753L
Protein MettaloPhosphatases Buffer	NEB	Cat#B0761
Bio-Rad Protein Assay Dye Reagent Concentrate	Bio-Rad	Cat#5000-0006
Biotin	Sigma-Aldrich	Cat#B4501
Glycerol (beta-) phosphate disodium salt	Sigma-Aldrich	Cat#50020
Critical commercial assays		
Pierce BCA Protein Assay Kit	Thermo Scientific	Cat#23225
WesternBright ECL	Advansta	Cat#K12049-D50
SuperSignal West Femto Chemiluminescent	Thermo Scientific	Cat#34096
Deposited data		
PPPome activity enrichment MS-RAW files	ProteomeXchange	PXD022383
global phosphoproteomics MS-RAW files	ProteomeXchange	PXD022303
OBIKA MS-RAW files	ProteomeXchange	PXD022759
Western blot RAW figures	Mendeley Data	https://doi.org/10.17632/4c4jcf27cp.1
Experimental models: Cell lines		
DKO MEFs (Figures 1, 2, 3, and 4B)	Wu et al., 2020	N/A
ULK1 MEFs (Figures 1, 2, and 4B)	Wu et al., 2020	N/A
A549 (Figures 2, 4C, 4D, 5G, S1, S2, S6A, and S7)	ATCC	CRM-CCL-185
HeLa	ATCC	CRM-CCL-2
SHA-ULK1 HeLa (Figure 3)	This study	N/A

(*Continued on next page*)

Continued

REAGENT or RESOURCE	SOURCE	IDENTIFIER
SHA-ULK1 D165A HeLa (Figure 3)	This study	N/A
VC HeLa (Figures 4E, 5A–5D, 5L, 5M, and S8A)	This study	N/A
SHA-STRN HeLa (Figures 4E, 5, and S8A)	This study	N/A
SHA-STRN S227A HeLa (Figures 5H–5M)	This study	N/A
SHA-STRN S227D HeLa (Figures 5H–5M)	This study	N/A
SHA-STRN L224A HeLa (Figure 5F)	This study	N/A
shSTRN HeLa (Figure S8C)	This study	N/A
VC Caco2 (Figures S8B, S8D, and S8E)	This study	N/A
SHA-STRN Caco2 (Figures S8B, S8D, and S8E)	This study	N/A
MCF7 (Figure S6B)	ATCC	HTB-22
MCF7 ATG7 KO clone 1 (Figure S6B)	This study	N/A
MCF7 ATG7 KO clone 2 (Figure S6B)	This study	N/A
Recombinant DNA		
Modified pCW57.1, SV40-Puromycin was replaced with MND-Blasticidin	This study	N/A
pLKO.1	Wiederschain et al., 2009	Addgene 21915
ULK1	Löffler et al., 2011	N/A
ULK1 D165A	Löffler et al., 2011	N/A
STRN-isoform-II	genomics-online.com	Cat#ABIN3986511
ATG7-CRISPR plasmid	O'Prey et al., 2017	N/A
Software and algorithms		
ImageJ	NIH	https://imagej.nih.gov/ij/index.html
Photoshop	Adobe	https://www.adobe.com/
MaxQuant	Cox and Mann, 2008	https://maxquant.net/maxquant/
Perseus	Tyanova et al., 2016	https://maxquant.net/perseus/
Cytoscape	Shannon et al., 2003	https://cytoscape.org/
ClueGO	Bindea et al., 2009	https://apps.cytoscape.org/apps/cluego
Motif Analysis	NIH	https://www.phosphosite.org/staticMotifAnalysis.action
Clustal Omega	Madeira et al., 2019	https://www.ebi.ac.uk/Tools/msa/clustalo/
Skyline	MacLean et al., 2010	https://skyline.gs.washington.edu/project/home/software/Skyline/begin.view
Difflogo	Nettling et al., 2015	https://bioconductor.org/packages/release/bioc/html/DiffLogo.html

RESOURCE AVAILABILITY

Lead contact

Further information and requests for materials, resources, and reagents should be directed to and will be fulfilled by the Lead Contact, Jörn Dengjel (joern.dengjel@unifr.ch).

Materials availability

All unique/stable reagents, i.e., plasmids and cell lines, generated in this study are available from the Lead Contact without restriction.

Data and code availability

Proteomic data have been deposited at PRIDE DB and are publicly available as of the date of publication. Accession numbers are listed in the Key resources table. Raw western blot and imaging data are deposited on Mendeley Data and are publicly available as of the date of publication. DOI is listed in the Key resources table.

This paper does not report original code.

Any additional information required to reanalyze the data reported in this paper is available from the lead contact upon request.

EXPERIMENTAL MODEL AND SUBJECT DETAILS

All cell lines used in this study were genotyped prior use and regularly tested negative for mycoplasma. Following cell lines were used mouse embryonic fibroblasts (MEFs), A549 lung carcinoma cells (ATCC, CCL-185), HeLa cervix adenocarcinoma cells (ATCC, CCL-2), CaCo-2 colorectal adenocarcinoma cells (ATCC, HTB-37) and MCF7 breast adenocarcinoma cells (ATCC, HTB-22). Cells were cultured in DMEM (10% FBS, 1% penicillin/streptomycin) at 37°C and 5% CO2.

METHOD DETAILS

Recombinant DNA constructs and virus production

Striatin (*STRN*) cDNA (isoform-2) was obtained from genomics-online company and *ULK1*^{WT}, *ULK1*^{D165A} (kinase dead) plasmids were previously described (Löffler et al., 2011). Note that Ser227 corresponds to Ser215 in Strn isoform-2. Strep-Tactin-HA tag (SHA) was fused N-terminal to *STRN, ULK1*^{WT} and *ULK1*^{D165A}, cloned into pCW57.1 vector (modified vector with MND-Blasticidin instead of hPGK-Puromycin) using Gibson assembly (NEB) for ectopic expression under doxycycline (2 ng/ml) inducible promoter. Phosphomutants (S215D and S215A) and motif mutant L212A of *STRN* were cloned in the same way as wild-type *STRN*. For inducible shRNA-based knock down of STRN, the vector pLKO.1 (Addgene, 21915) was used. Following striatin shRNA sequence (TRCN0000036947) was chosen from the Broad RNAi consortium: Forward sequence: 5'-CCGGCGTCATTGATACTTCAACAATCTCGAGATTGTTGAAGTATCAATGACGTTTTTG-3', Reverse sequence: 5'-AATTCAAAAACGTCATTGATACTTCAACAATCTCGAGATTGTTGAAGTATCAATGACG-3'. As negative control a shRNAs targeting luciferase was used. Respective constructs cloned into lentiviral vectors were co-transfected with packaging and envelope plasmids using jetPRIME reagent (polyplus transfection) in HEK293T cells. Fresh DMEM was supplemented to cells 6 hours post transfection. After 24 hours, the culture supernatant was filtered using 0.22 μm filter and 8 μg/ml of polybrene was supplemented before infecting recipient cells. Stable cell-lines were generated using blasticidin selection (5 μg/ml for 6 days) in respective cell lines containing the required vector. *STRN*^{WT} and phosphomutants were ectopically expressed in HeLa cells and *ULK1*^{WT}, *ULK1*^{D165A} were expressed in *ULK1* knockout HeLa cells.

ULK1 and ULK1^{D165A} protein purification

ULK1$^{-/-}$ HeLa cells expressing *SHA-ULK1*^{WT} and *SHA-ULK1*^{D165A} were grown in 20x15 cm dishes for each construct. Before harvesting, cells were treated with HBSS with concanamycin A (conA, 2 nM, Santa Cruz) for 1 hour. Cell lysates were obtained using modified-RIPA (150 mM NaCl, 50 mM Tris-HCl, 1 mM EDTA, 1% NP-40, 0.1% sodium deoxycholate, and EDTA-free protease inhibitor and PhosSTOP) as lysis buffer. Immunoprecipitations were carried out using 2 mL of Strep-Tactin® XT-4Flow slurry for each protein purification. Lysates were incubated with beads equilibrated with lysis buffer at 4°C overnight in a rotor. Beads were washed three times with lysis buffer before eluting proteins with 3 × 200 μL of 100 mM biotin containing elution buffer (50 mM Tris-HCl, pH 7.5, 100 mM NaCl, 0.05% Tween-20, 20% glycerol and 3 mM DTT). All steps were performed at 4°C.

Cell culture and treatments

Ulk1/ulk2 double knock out (DKO) MEFs were kindly provided by Tullia Lindsten (Memorial Sloan Kettering Cancer Center, New York, USA). *Ulk1/ulk2* DKO MEFs transfected with empty vector or cDNA encoding FLAG-tagged human *ULK1* have been described previously (Wu et al., 2020). Briefly, the vectors pMSCVpuro or pMSCVpuro/FLAG-*hULK1* were transfected into Plat-E cells (kindly provided by Toshio Kitamura, Institute of Medical Science, University of Tokyo, Japan) using FuGENE® 6 (Promega; E2692). After 48 h, retroviral supernatant was collected and used for the infection of *ulk1/ulk2* DKO MEFs in combination with 10 μg/mL polybrene (Sigma-Aldrich; H9268-106). After 12 h, cells were selected in medium containing puromycin (2.5 μg/mL). Following selection, single cell clones used in this study were obtained by limiting dilution.

For SILAC-labeling, cells were grown in SILAC-DMEM, supplemented with 10% dialyzed FBS 1% penicillin/streptomycin and 1% GlutaMax, containing non-labeled or labeled arginine and lysine variants: Lys0 and Arg0 for light, Lys4 and Arg6 for medium as well as Lys8 and Arg10 for heavy. The final concentration of arginine was 42 mg/L, and of lysine was 73 mg/L. A final concentration of 26 mg/L L-proline was added to avoid arginine to proline conversion. Cells were split and culture media were changed 18 hours before treatments. Cells were incubated with either DMSO (vehicle), 200 nM rapamycin, 2 nM conA or 1 μM MRT6892 in DMEM or in HBSS. Cells were washed once with PBS before HBSS treatment. All treatments were incubated for 1 hour before harvesting cells. For inducible and empty vector control cell lines, protein expression was induced by adding 2 ng/ml doxycycline 20 hours before treatments. After treatment, cells were washed twice with ice-cold PBS, scraped and collected in tubes, followed by centrifugation to pellet cells. Supernatant were discarded and cell pellets were stored in −80°C for further use.

Cell lysis

For immunoblotting, cell pellets from 1x10 cm dish were lysed in 200 μL of lysis buffer (50 mM Tris-HCl, pH 7.6, 150 mM NaCl, 1 mM EDTA, 1% NP-40, 2% SDS, and benzonase 1:5000). For immunoprecipitation, cell pellets from one 15 cm dishes were lysed in 800 μL of modified RIPA buffer (50 mM Tris-HCl, pH 7.6, 150 mM NaCl, 1 mM EDTA, 1% NP-40, 0.1% sodium deoxycholate, EDTA-free protease inhibitor and PhosSTOP). For PPPome enrichment, cell pellets from 2x15 cm dishes were lysed in 1.6 mL of phosphatase pulldown buffer (50 mM Tris-HCl, pH 7.5, 500 mM NaCl, 5 mM beta-glycerophosphate, 0.5% Triton X-100, 0.1 mM DTT, and

EDTA-free protease inhibitor) at a total protein concentration of 1 mg/mL (Lyons et al., 2018). For phosphoproteome and PRM analyses, cell pellets from 4x15 cm dishes were lysed in 8 M Urea in 50 mM Tris-HCl pH 8.0. Lysates were sonicated three times for 10 s on ice and centrifuged at 21,000 × g at 4°C for 15 min. Protein concentration was determined by BCA assay. Protein amounts were adjusted to equal concentrations with lysis buffer for all samples.

Immunoblotting

Protein extracts were mixed with 6 x Laemmli buffer (0.375 M Tris pH 6.8, 12% SDS, 60% glycerol, 0.6 M DTT, 0.06% bromophenol blue) to 1x and incubated at 75°C for 10 min. 30 μg of total protein from each sample were separated by SDS-PAGE using homemade gels. Separated proteins were transferred to a nitrocellulose membrane for proteins larger than 30 kDa or a PVDF membrane for proteins smaller than 30 kDa for 30 min using Trans-Blot® Turbo transfer system (BIO-RAD, 1704150) or for 2 hours using wet transfer system under a constant electric current. Membranes were blocked by either 5% milk or 5% BSA in TBS-T (10 mM Tris, 150 mM NaCl and 0.1% Tween-20). Membranes were incubated overnight at 4°C with respective primary antibodies. Membranes were washed thrice with TBS-T before incubating with peroxidase-conjugated secondary antibodies for 1 hour. Blotted proteins were visualized using either SuperSignal West Femto Chemiluminescent or WesternBright ECL and the Odyssey® Fc reader (LI-COR Biosciences - GmbH). Antibodies against β-actin were used to quantify and normalize protein amounts. Densitometry measurements were performed using ImageJ 1.53d (Wayne Rasband, National Institutes of Health).

Immunostainings and fluorescence microscopy

For immunofluorescence, the indicated cells were seeded on collagen I (ThermoFisher, A10483-01, diluted in 0.02M acetic acid to 50ug/ml)-coated coverslips 24 h prior to experiments. The next day, cells were treated as indicated and fixed using ice-cold 100% methanol (MetOH) for 10 min. Fixed cells were washed 6 times in PBST, blocked in PBST containing 5% horse serum (ThermoScientific, 16050) for 30 min, and finally washed 6 times in PBST. Cells were incubated in a wet chamber with a primary antibody solution, overnight at 4°C. Cells were then washed 6 times in PBST and incubated in the secondary antibody solution in the dark, for 2 h at room temperature. After incubation, cells were washed 6 times with PBST, incubated in 10 μM Hoechst 33342 solution (Sigma-Aldrich, 14533) for 1 min, washed again 6 times, and embedded in ProLong Gold antifade reagent (ThermoFisher, P36931). Confocal imaging was performed using a Leica STELLARIS 8 FALCON system. Images were analyzed, quantified, and prepared with Fiji employing intensity thresholding, size exclusion, and noise filtering, based on signal intensities of the ConA control. For quantification of p62/SQSTM1 dots cells with high background were manually excluded. Per condition around 60-90 cells were analyzed.

Affinity purification

Affinity purification (AP) was performed by KingFisher Duo Prime System (ThermoFisher). Briefly, 80 μL of anti-HA magnetic beads slurry were washed with modified RIPA and incubated with lysate for 1 hour at RT. The beads were washed three times in modified RIPA before elution followed by FASP sample processing as described (Wiśniewski et al., 2009). Briefly, beads were loaded on the 10 KD cut-off filter, spun (6000 g, 10 min) and proteins were reduced with 1 mM DTT in 8 M urea/100 mM ABC buffer for 20 min at RT followed by alkylation using 1 mM IAA in 8 M Urea/100 mM ABC Buffer for 20 min in the dark at RT. Urea was replaced by 50 mM ABC buffer, Trypsin was added (trypsin:protein ratio = 1:100) and proteins digested overnight at 37°C. The next day peptides were spun down and purified by STAGE tips.

PPPome activity enrichment

Phosphatase inhibitor beads (PIB) were synthesized as described previously (Lyons et al., 2018). with following modifications: 1.5 g (per mg of MCLR used) of NHS-activated Sepharose beads were washed with 3 × 5 mL of 1 mM HCl followed by 2 × 5 mL of coupling buffer (100 mM NaHCO3, pH 8.2). Aminoethanethiol-MCLR was resuspended in 100 μL of methanol and coupled to the activated beads in coupling buffer for 1.5 h at room temperature. To enrich phosphatases based on their activity, lysates were incubated with 20 μL of solid packed PIB resin at 4°C on a rotor. After 2 hours, PIBs were spun down and washed 3 x with phosphatase pulldown buffer. Proteins bound to beads were either digested in solution (for MEFs) or eluted twice using 2 x Laemmli buffer at 75°C followed by in-gel digestion (for A549).

In vitro kinase assay

For OBIKA, cell pellets were lysed in primary amine-free lysis buffer (50 mM HEPES pH 8.0, 1% NP-40, 150 mM NaCl, 0.1% sodium deoxycholate, 1 x EDTA-free protease inhibitor) and centrifuged at 4000 rpm for 10 min at 4°C. Total protein amount was quantified by BCA assay and 100 μl of lysate was kept as input. According to binding tests (Figure S3), 300 μl of beads can bind 2 mg of protein. 5 mL of NHS-activated Sepharose beads were washed with 3 × 10 mL of ice cold 1 mM HCl and 2 × 10 mL of lysis buffer before incubating with 60 mg protein to saturate beads. The coupling was performed on a rotor at 4°C overnight. Next, beads were spun down to remove supernatant (flow-through). The total protein amount of both input and flow-through was measured by BCA assay or analyzed by SDS-PAGE. Beads were washed with 3 × 10 mL of phosphatase buffer (50 mM HEPES, 100 mM NaCl, 0.1% NP-40). 1 mL of phosphatase buffer containing 5,000 to 10,000 units of lambda phosphatase with 1 mM MnCl2 was added and incubated for 4 hours at room temperature or overnight at 4°C on the rotor to dephosphorylate endogenous proteins. Beads were washed with 2 × 10 mL of kinase buffer (50 mM Tris-HCl pH 7.6, 10 mM MgCl2, 150 mM NaCl and 1x PhosSTOP). Endogenous kinases bound to

beads were inhibited by incubation with 1 mM FSBA in 1 mL of kinase buffer at RT on the rotor for 2 hours. In addition, straurosporine was added to a final concentration of 100 μM to inhibit the remaining active kinases for 1 hour. The beads were washed with 3 × 10 mL of kinase buffer to remove non-bound kinase inhibitors. The supernatant was removed completely by gel loading tips. Kinase buffer was added to a total volume of 900 μL for ATP only control samples and 800 μL for both kinase dead and WT ULK1 samples. 100 μl of 10 mM ATP and 10 μL of 100 mM DTT were added into each tube and 100 μl of purified kinases were added to kinase dead and WT ULK1 samples. Kinase assays were performed on a rotor at 37°C for 4 hours. Finally, reactions were quenched by adding 0.96 g urea into each tube, followed by protein digestion, fractionation, and phosphopeptides enrichment.

For purified STRN kinase assays, $STRN^{WT}$ and $STRN^{L212A}$ were purified by anti-HA magnetic beads. Beads were incubated with either purified WT or kinase dead ULK1 in kinase buffer (50 mM Tris-HCl pH 7.6, 10 mM MgCl2, 150 mM NaCl, 1x PhosSTOP, 1 mM DTT and 1 mM γ-[18O4]-ATP). The assay was stopped by the addition of 8 M urea followed by protein digestion

Protein digestion and sample preparation for MS

For affinity purifications and purified STRN, beads were mixed with 8 M urea and 1 mM DTT and transferred onto 10 kDa MW cut-off filter. Protein digestion for MS analysis was performed overnight according to the FASP protocol (Wiśniewski et al., 2009). On day 2, peptides were eluted twice with 200 μL 50 mM ammonium bicarbonate into fresh tubes. Eluates were acidified with 5 μL TFA to a final concentration of 1%. Eluates of AP samples were desalted by STAGE tips. Eluates of *in vitro* kinase assay samples were frozen, lyophilized prior to phosphopeptide enrichment.

For *in vivo* phosphoproteome and OBIKA samples, lysates or proteins on beads were reduced by 1 mM DTT, alkylated by 5 mM iodoacetamide, and digested by Lys-C for 4 h. The concentration of urea was diluted to 1 M before overnight trypsin digestion. The peptides were purified and fractionated as described previously (Hu et al., 2019). Briefly, peptides were purified by SPE using HR-X columns in combination with C18 cartridges. The purified peptides were frozen, lyophilized and fractionated by HpH reversed phase chromatography (Batth et al., 2014). 96 fractions were mixed with an interval of 12 to yield 12 final fractions. The peptides were acidified, frozen in liquid nitrogen and lyophilized prior to phosphopeptides enrichment.

For phosphopeptides enrichment, samples were incubated with 2 mg TiO_2 slurry, which were pre-incubated with 300 mg/mL lactic acid in 80% acetonitrile, 1% TFA prior to enrichment (Zarei et al., 2016) for 30 min at room temperature. For peptide elution, TiO_2 beads were transferred to 200 μL pipette tips, which were blocked by C8 discs. Tips were sequentially washed with 200 μL of 10% acetonitrile/1% TFA, twice 200 μL of 80% acetonitrile/1% TFA, and 100 μL of LC-MS grade water. Phosphopeptides were eluted with 50 μL of 1.25% ammonia in 20% acetonitrile and 50 μL of 1.25% ammonia in 80% acetonitrile into single tubes. Eluates were acidified with 5 μL of formic acid. Samples were concentrated by vacuum concentration and resuspended in 20 μL of 0.1% formic acid for LC-MS/MS analysis. The tip flow-through was desalted by STAGE tips for non-phosphopeptide analysis.

PRM assays

A549 cells were starved for up to 60 min in HBSS. Lysates were digested by Lys-C for 4 hours and trypsin overnight. Peptides were purified by STAGE tips. Phosphopeptides were enriched as outlined above in the section *Protein Digestion and Sample Preparation for MS.* The tip flow-through was desalted by STAGE tips for protein analysis. STRN Ser227 phosphorylation was relatively quantified using a parallel-reaction monitoring (PRM) assay using standard settings.

LC-MS/MS analyses

LC-MS/MS measurements were performed on a QExactive (QE) Plus and HF-X mass spectrometer coupled to an EasyLC 1000 and EasyLC 1200 nanoflow-HPLC, respectively (all Thermo Scientific). Peptides were fractionated on a fused silica HPLC-column tip (I.D. 75 μm, New Objective, self-packed with ReproSil-Pur 120 C18-AQ, 1.9 μm (Dr. Maisch) to a length of 20 cm) using a gradient of A (0.1% formic acid in water) and B (0.1% formic acid in 80% acetonitrile in water): samples were loaded with 0% B with a max. pressure of 800 Bar; for OBIKA, peptides were separated by 2%–25% B within 85 min with a flow rate of 250 nL/min, and for the rest of experiments, peptides were separated by 5%–30% B within 85 min with a flow rate of 250 nL/min. For PRM assays, phosphopeptides were separated by 25%–33% B within 35 min, and non-phosphopeptides were separated by 10%–30% within 41 min with a flow rate of 250 nL/min. Spray voltage was set to 2.3 kV and the ion-transfer tube temperature to 250°C; no sheath and auxiliary gas were used. Mass spectrometers were operated in the data-dependent mode; after each MS scan (mass range m/z = 370 – 1750; resolution: 70'000 for QE Plus and 120'000 for HF-X) a maximum of ten, or twelve MS/MS scans were performed using a normalized collision energy of 25%, a target value of 1'000 (QE Plus)/5'000 (HF-X) and a resolution of 17'500 for QE Plus and 30'000 for HF-X. MS raw files were analyzed using MaxQuant (version 1.6.2.10) (Cox and Mann, 2008) using a Uniprot full-length *Homo sapiens* (March, 2016), *Mus musculus* database (April, 2016) plus human ULK1 and common contaminants such as keratins and enzymes used for in-gel digestion as reference. Carbamidomethylcysteine was set as fixed modification and protein amino-terminal acetylation, serine-, threonine- and tyrosine- (heavy) phosphorylation, and oxidation of methionine were set as variable modifications. The MS/MS tolerance was set to 20 ppm and three missed cleavages were allowed using trypsin/P as enzyme specificity. Peptide, site, and protein FDR based on a forward-reverse database were set to 0.01, minimum peptide length was set to 7, the minimum score for modified peptides was 40, and minimum number of peptides for identification of proteins was set to one, which must be unique. The "match-between-run" option was used with a time window of 0.7 min. MaxQuant results were analyzed using Perseus (Tyanova et al., 2016). For PRM assays, the m/z of peptides were listed in an inclusion list. MS/MS scans were performed using a normalized collision

energy of 25%, a maximum target value of 100'000 and a resolution of 35'000 for QE Plus and 30'000 for HF-X. MS raw files were analyzed using Skyline (MacLean et al., 2010).

MS-based proteomics data have been deposited to the ProteomeXchange Consortium via the PRIDE partner repository (Perez-Riverol et al., 2019). (a) PPPome activity enrichment: identifier PXD022383; (b) global phosphoproteomics: identifier PXD022303; (c) OBIKA: identifier PXD022759.

QUANTIFICATION AND STATISTICAL ANALYSES

The *in vivo* phosphoprotome data were analyzed as described (Hu et al., 2019). Briefly, measurements of the log2 fold changes on each site were combined into a random effect model, considering *a priori* the sites as a random effect and including the variability among replicates by also considering the replicates as a random effect. The model assigns an average effect size and its corresponding 95% confidence interval to each site. If the confidence interval includes values of zeros, then there is no statistically significant log2 fold change, whereas if the confidence interval is above (below) zeros, there is statistical evidence for upregulation (downregulation). Additionally, significant outliers (significance A) were determined by Perseus using the fitted values of the random effect model. Briefly, shortlisted significant regulated phosphosites had to fulfill both selection criteria: (a) their average fold change had to be significant as determined by the random effect model taking the variability among biological replicates, sites, and the number of replicates for each site into account ($p < 0.05$); and (b) the average fold change had to be an outlier as determined by significance A ($p < 0.05$).

OBIKA data were analyzed using Perseus. Missing values in control experiments were replaced by random values of a normal distribution to mimic low abundance measurements. Both width and down shift were applied according to default settings. Replacement of missing values was applied to each expression column separately. Replicates were grouped and significant changes determined (FDR $\leq$ 0.05).

GO-term analyses were performed with Cytoscape 3.8.0 (Shannon et al., 2003), and ClueGO 2.5.7 (Bindea et al., 2009). Ontology enrichment (background: genome) was calculated using those genes, whose proteins carried phosphosites that were statistically significantly regulated, either positive or negative. GO-biological process (BP), and -molecular function (MF) were selected for calculations. GO term fusion was used. Only pathways with a p value $\leq$ 0.01 were determined as significant (Bonferroni corrected). GO tree interval was set between 4 and 5. GO clusters contained at least 3 (HBSS/DMEM), 20 (ULK1/DKO) genes or 2% (HBSS/DMEM), 10% (ULK1/DKO) of all input genes. Enrichment/depletion (two-sided hypergenometric test) and Bonferroni p value correction were selected for statistical analyses. Sequence logos and motif analyses were performed using the service of the PhosphoSitePlus® website. The background for both calculations was based on the respective input sequences. Homolog sequences alignments were performed with Clustal Omega, a web tool of EMBL-EBI, using default settings (Madeira et al., 2019). Protein homologs were extracted from UniProt. Phosphatase binding proteins were connected to known interactors using the STRING database.

Cell Reports, Volume *36*

Supplemental information

ULK1 phosphorylation of striatin activates protein phosphatase 2A and autophagy

Zehan Hu, Devanarayanan Siva Sankar, Bich Vu, Alexandre Leytens, Christine Vionnet, Wenxian Wu, Michael Stumpe, Esther Martínez-Martínez, Björn Stork, and Jörn Dengjel

Supplemental Figure S1

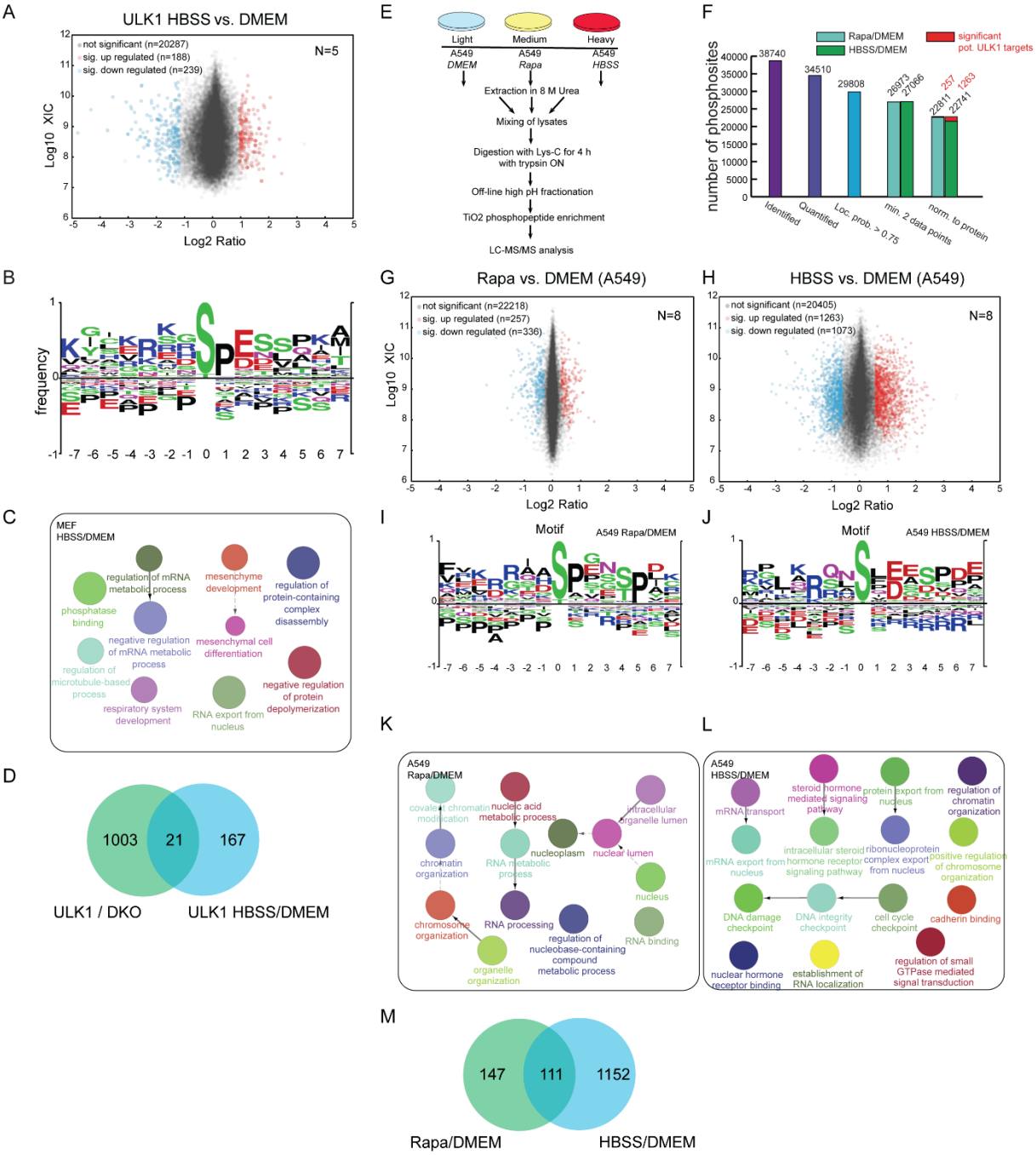

Supplemental Figure S1: Global *in vivo* phosphoproteomic approaches to identify potential ULK1 target sites in ULK1 MEFs (A-D) and A549 cells (E-M). Related to Figure 1 and 2. (A) Regulation of phosphosites of ULK1 MEFs kept for 1 h in HBSS compared to DMEM. Average intensities based on the summed extracted ion currents (XIC) of peptides carrying respective phosphosites are shown in relation to the fold change of regulation (log2 SILAC ratio) of five biological replicates. Significantly regulates sites are marked in color ($p<0.05$, BH corrected). **(B)** Motif analysis of significantly positively regulated phosphosites of ULK1 MEFs kept for 1 h in HBSS compared to DMEM highlighted in panel (A). **(C)** GO network of proteins carrying significantly positively regulated sites highlighted in panel (A). **(D)** Overlap of significantly dysregulated sites between the two indicated MEF experiments (five biol. replicates each). **(E)** SILAC-based quantitative MS workflow. Human A549 lung

adenocarcinoma cells were used to identify phosphosites potentially being regulated by ULK1 by comparing cells kept in fed conditions (DMEM) to starved cells (HBSS, 1 h) or cells treated with rapamycin (200 nM, 1 h). **(F)** Number of identified and quantified phosphosites fulfilling the indicated criteria comparing (i) A549 cells treated with rapamycin to non-treated cells, and (ii) A549 cells kept for 1 h in HBSS compared to DMEM. **(G-H)** Regulation of phosphosites of A549 cells treated for 1 h with rapamycin compared to non-treated cells (G), or starved A549 cells (HBSS) compared to non-starved cells (DMEM) (H). Shown are average intensities based on the summed extracted ion currents (XIC) of peptides carrying respective phosphosites in relation to the fold change of regulation (log2 SILAC ratio) of eight biological replicates. Significantly regulates sites are marked in color ($p<0.05$). **(I-J)** Motif analysis of significantly positively regulated phosphosites of A549 cells treated with rapamycin (I), or starved (J) compared to non-treated cells (DMEM). **(K-L)** GO network of proteins carrying significantly positively regulated sites after rapamycin treatment (K) or starvation (L). **(M)** Overlap of significantly dysregulated sites between the two indicated A549 experiments (eight biol. replicates each).

Supplemental Figure S2

A

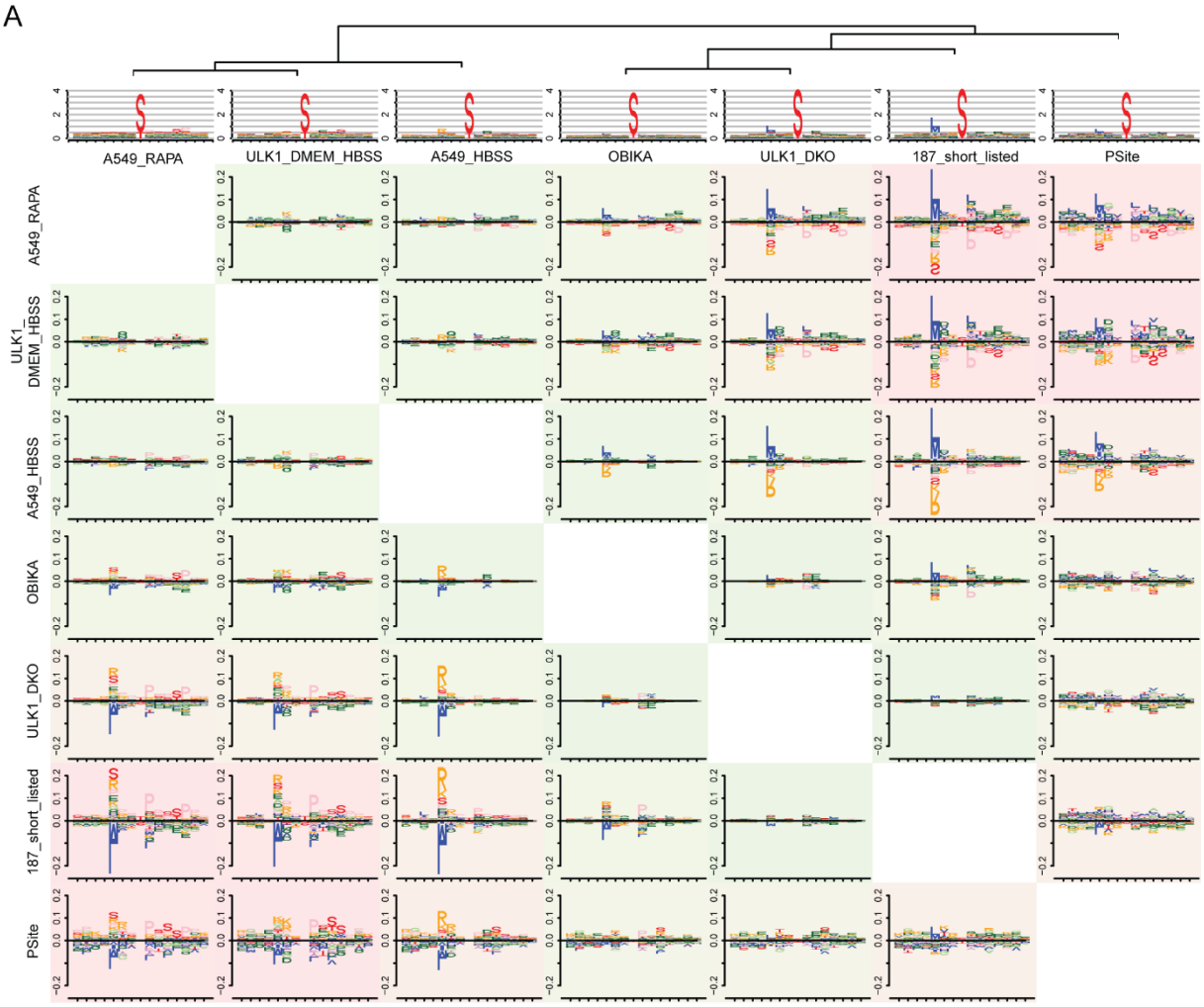

B

	neg ctrl	A549_HBSS	OBIKA	A549_RAPA	ULK1_DMEM_HBSS	Psite	187 short listed	ULK1_DKO
ULK1_DKO	2.29	0.70	0.33	1.15	1.03	0.94	0.31	0.00
187 short listed	2.72	1.20	0.69	1.70	1.61	1.18	0.00	
Psite	2.32	1.26	0.86	1.65	1.69	0.00		
ULK1_DMEM_HBSS	2.60	0.55	0.69	0.57	0.00			
A549_RAPA	2.75	0.53	0.70	0.00				
OBIKA	1.84	0.40	0.00					
A549_HBSS	2.23	0.00						
neg ctrl	0.00							

Supplemental Figure S2: Similarity analysis comparing the published ULK1 motif with motifs generated in this study. Related to Figure 1, 3, and S2. (A) DiffLogo was used to plot pair-wise difference logos displaying distances between each motif (green background color = similar; red = dissimilar). Sequence logos of each motif and leaf-ordered cluster tree are also plotted. **(B)** Distances between logos as indicated by the cluster tree in panel A. Psite: published ULK1 motif on https://www.phosphosite.org/. As negative control (neg ctrl) a uniform distribution of the 20 proteinogenic amino acids over all positions was used.

Supplemental Figure S3

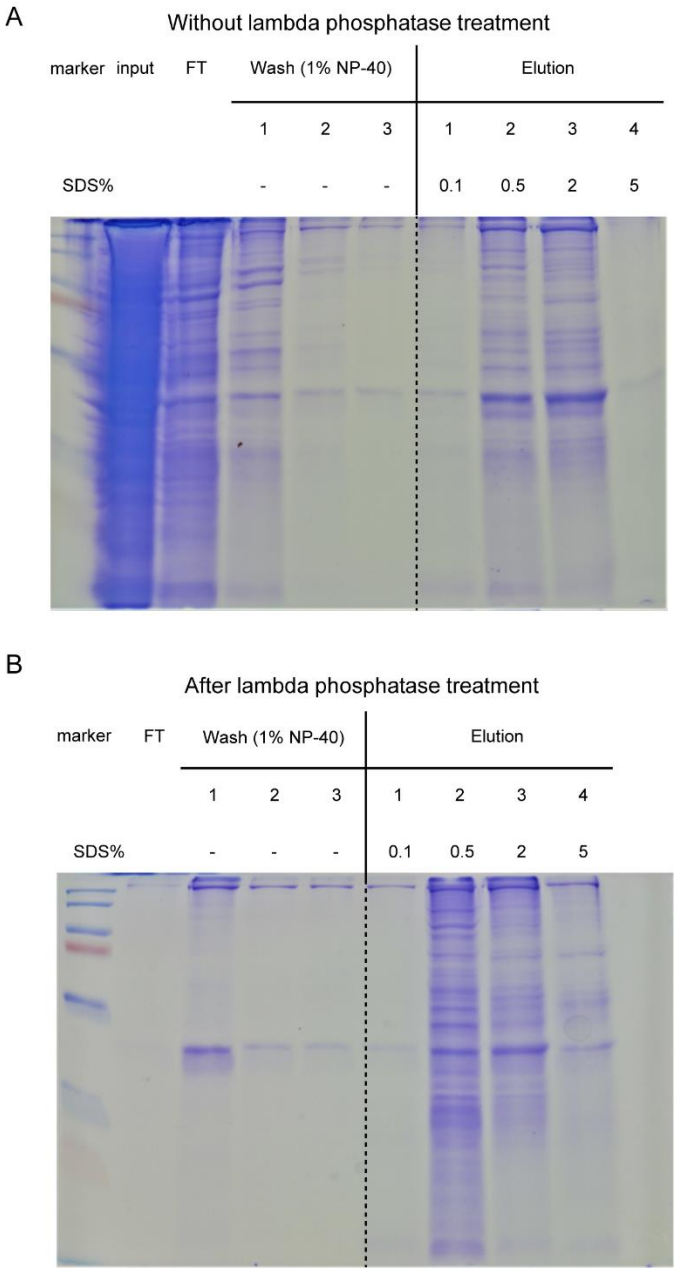

Supplemental Figure S3: SDS-PAGE analyses highlight native conditions of on bead *in vitro* kinase assays. Related to Figure 3. (A) Multimeric protein complexes are bound to NHS beads via primary amino groups in a mild lysis buffer containing 1% NP-40. After three washes no additional proteins are removed from the beads. The addition of the strong denaturing agent SDS to the lysis buffer leads to elution of additional proteins. **(B)** Lambda phosphatase treatment does not interfere with binding of native protein complexes to NHS beads. Addition of SDS to the lysis buffer does still lead to elution of non-covalently bound proteins.

Supplemental Figure S4

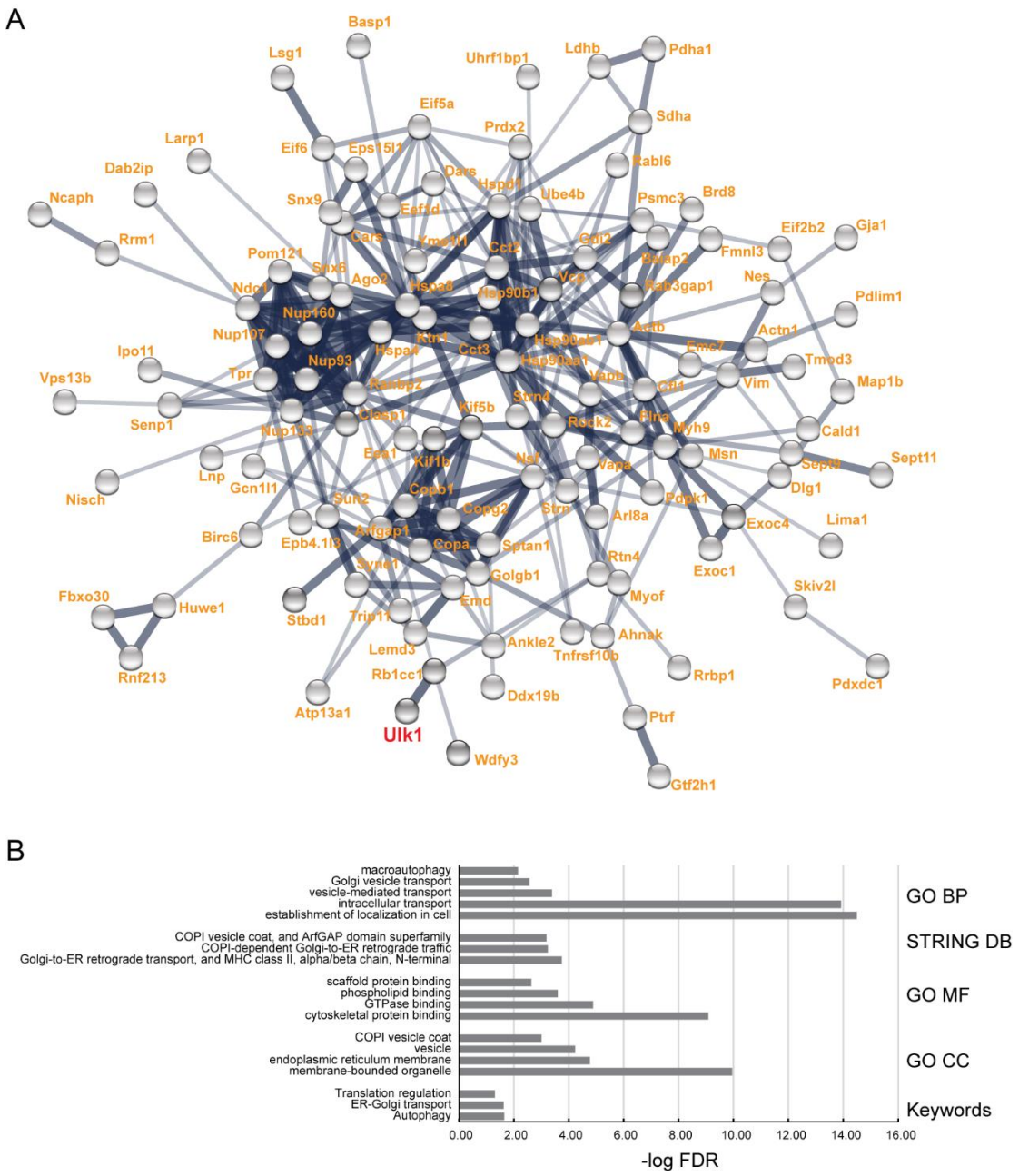

Supplemental Figure S4: Interaction analysis of newly identified ULK1 target proteins. Related to Figure 3. (A) STRING DB was used to analyze known protein-protein interactions of the newly identified 157 bon fide ULK1 targets (Table S4). An interaction network of 118 proteins including ULK1 could be generated. Thickness of edges indicates confidence of interaction. Proteins are represented by nodes. **(B)** Examples of significantly enriched pathways and processes linked to proteins in the network highlight the function of ULK1 in vesicle generation and transport. GO: gene ontology; BP: biological process; MF: molecular function; CC: cellular component.

Supplemental Figure S5

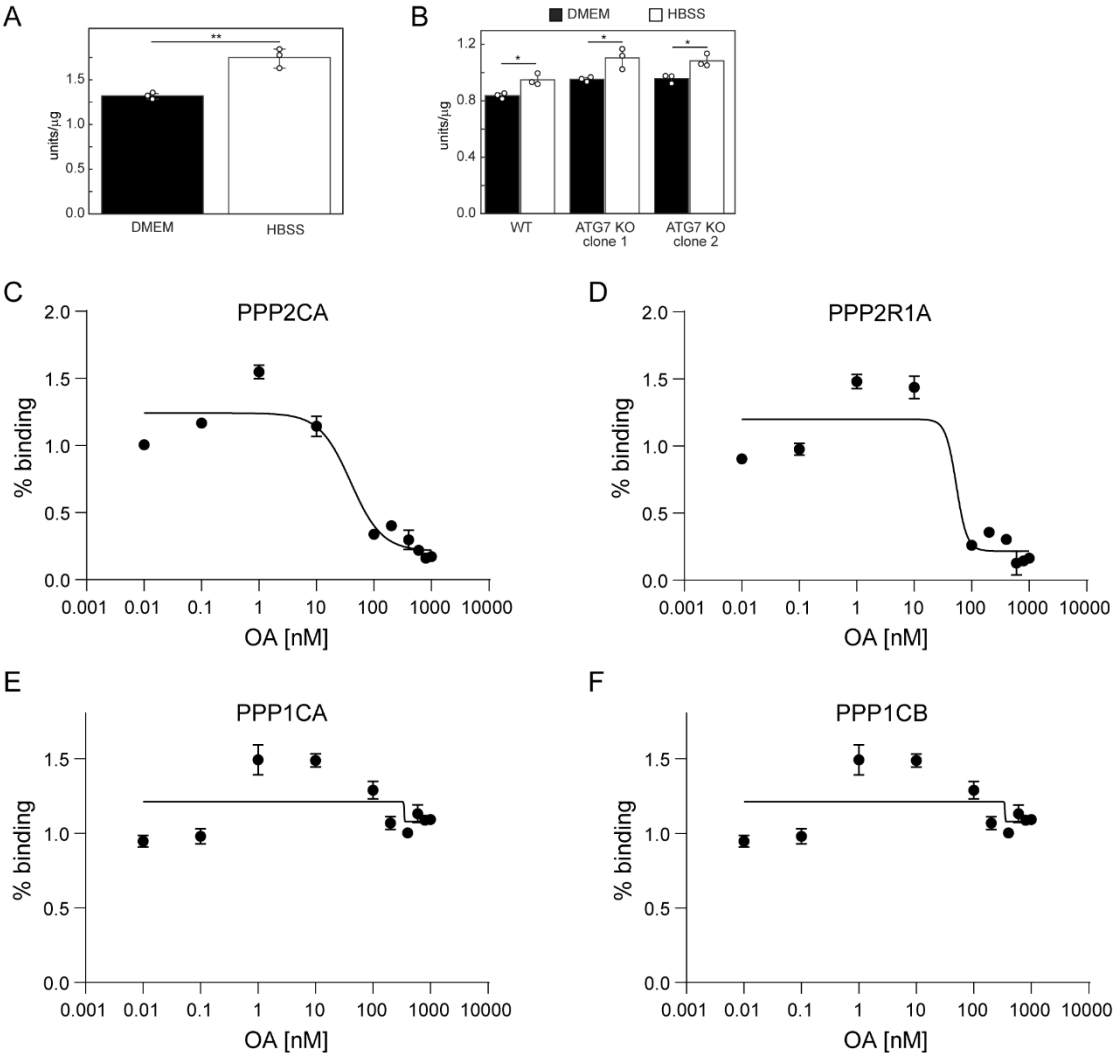

Supplemental Figure S5: Altered phosphatase activity in autophagy conditions. Related to Figure 4. (A) Increased phosphatase activity in starved A549 cells. p-Nitrophenyl phosphate was employed to study phosphatase activity due to culture conditions. Starvation conditions (HBSS) led to a 1.3fold increase of phosphatase activity compared to fed cells (DMEM). Phosphatase units are depicted per µg cellular proteins (n=3, T test, **: p<0.01). Error bars indicate 95% confidence intervals. **(B)** Increased phosphatase activity does not depend on functional autophagy. p-Nitrophenyl phosphate was employed to study phosphatase activity due to culture conditions in MCF7 WT and ATG7 KO cells. Starvation conditions (HBSS) led in all cases to a significant increase of phosphatase activity compared to fed cells (DMEM). Phosphatase units are depicted per µg cellular proteins (n=3, T test, *: p<0.05). Error bars indicate 95% confidence intervals. **(C-F) Activity-based enrichment of PP2A by microcystin-LR beads.** Whole cell lysates were incubated with increasing concentrations of okadaic acid (OA) for 1 h at RT followed by phosphatase enrichment using microcystin-LR coupled beads (n=3). Whereas OA interferes with binding of PP2A subunits in a concentration-dependent manner (C-D), the used concentrations do not interfere with PP1 subunit binding (E-F). Samples without OA were used to define 100% binding. Curve fitting was performed by nonlinear regression. Error bars indicate standard deviation.

Supplemental Figure S6

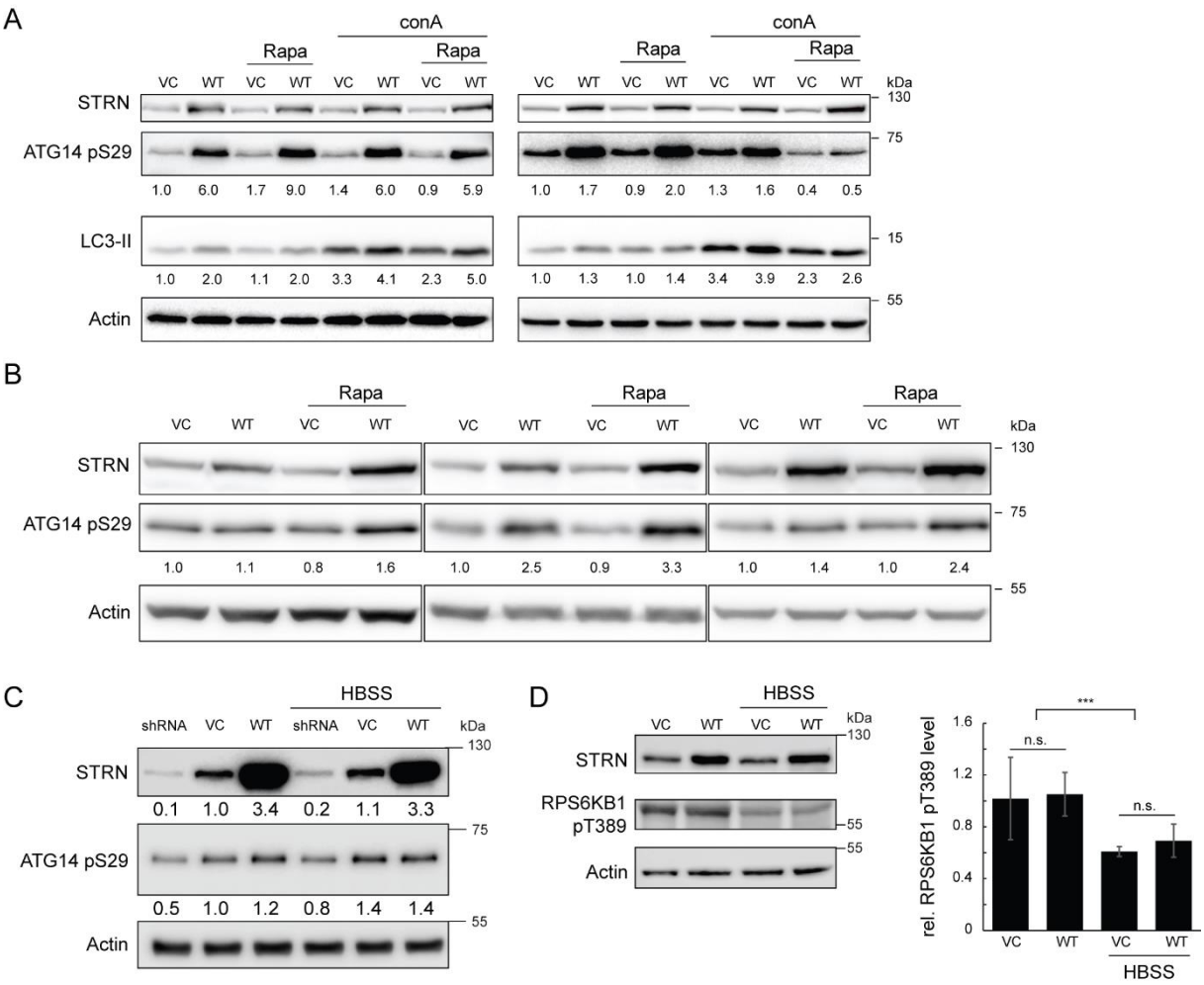

Supplemental Figure S6: Overexpression of STRN in human cancer cell lines leads to increased ULK1 activity as monitored by ATG14^{Ser29} phosphorylation. Related to Figure 5. (A) HeLa cells were treated with rapamycin (Rapa) and concanamycin A (conA) as indicated. Ectopic expression of WT STRN (WT) leads to increased ULK1 activity as analyzed by its target site Ser29 on ATG14. In agreement LC3 lipidation is increased indicating an increased autophagy flux. Actin was used as loading control. Vector control cells (VC) were used as negative control. Shown are two biological replicates. **(B)** Caco-2 cells were treated with rapamycin (Rapa) as indicated. Ectopic expression of WT STRN leads to increased ULK1 activity as analyzed by its target site Ser29 on ATG14. VC cells were used as negative control. Actin was used as loading control. Shown are three biological replicates. **(C)** shRNA-based knock down of endogenous STRN in HeLa cells leads to decreased ATG14 Ser29 phosphorylation, indicating reduced ULK1 activity. **(D)** Ectopic expression of WT STRN does not alter mTORC1 activity in Caco-2 cells as analyzed by RPS6KB1 phosphorylation. VC cells were used as negative control. Actin was used as loading control. Bar diagram shows quantification of three biological replica. n.s.: not significant; *** = p<0.001. Error bars indicate standard deviation.